Politecnico di Torino

FACOLTÀ DI INGEGNERIA
Corso di Laurea Magistrale in Ingegneria aerospaziale

Tesi di laurea magistrale

Multi-fidelity strategies for Navier-Stokes equations

Candidato:
Stefano Berlingeri
Matricola S265830

Relatore:
Prof.ssa Sandra Pieraccini

Anno Accademico 2020-2021

Abstract

Navier-Stokes equations, which are a set of partial differential equations, are the most used mathematical tool to describe fluid dynamics. Nowadays, the solution is obtained mainly through finite volume method implemented in computational fluid dynamics (*CFD*) software. An accurate fluid dynamics simulation could require a lot of computational efforts, which translates in high costs, especially in real industrial cases. On the other hand, a low fidelity simulation is usually faster and less time demanding but, of course, less accurate.

A multy-fidelity approach is applicable in those cases where the equations to be solved are dependent on one or more parameters. It allows to reconstruct a high fidelity solution, in any point of the parameter domain, suitably combining a large number of computationally inexpensive low fidelity simulations and a low number of high fidelity simulations. The computational cost strongly decreases in those cases where several high fidelity simulations at different points in the parameter domain are needed, such as in optimization problems and uncertainty quantification techniques.

Since for incompressible fluid dynamics problems the main parameter that we have to consider is the *Reynolds number* a bifidelity strategy is applied in some common fluid dynamics testcases and it is evaluated if the approach is applicable with satisfactory results.

CONTENTS

1 FLUID DYNAMICS EQUATIONS

As it is known, atoms and molecules are the fundamental constituents of matter. Atoms are composed of a nucleus, made of protons and neutrons, and one or more electrons that belong to orbitals somewhere around the nucleus. Tow or more atoms held together by chemical bonds form a molecule.

Also, matter can exist in different states, whose are solid, liquid, gas and plasma. Of our interest are liquid and gas, which are fluids: that means they don't possess an own shape and they can't resist to a shear force applied to them. In fact, in liquids, interaction forces of the consituent particles aren't strong enough to pack them together as in solids and they aren't so weak to leave them free to move indipendentely as in gases.

In this chapter we will review the property of fluids and show the equations that describe their behavior when a force is applied to them.

1.1 FLUID AS CONTINUOUS MEDIUM

We could think to describe the behavior of a fluid studying the motion of each constituent particle, but a simple analysis of their number discourages this approach in practical cases. We are interested in macroscopic properties of the fluid and, with this in mind, it is useful to think of a fluid as a *continuum medium* whose constituents are *fluid particles*. A fluid particle is a point-like elementary volume, but still wide enough to contain a number of particles sufficient to define statistics properties.

This can be acceptable if the continuum hypothesis is verified, which means that the average distance travelled by a constituent particle of the fluid (atom or molecule) before a collision, called

mean free path, is orders of magnitude smaller than the characteristic dimension of the fluid dynamic problem, namely

$$Kn := \frac{l_{mfp}}{L} << 1$$

where Kn is called the *Knudsen number*, l_{mfp} is the mean free path and L is the characteristic length of the problem. This is true in most pratical cases and, in paticular, in the problems that we are going to face up[1]. A fluid particle is therefore assimilable to a point and fluid properties are continuos functions in time and space.

1.1.1 Macroscopic properties of a fluid

Once the concept of fluid particle is defined, thermodynamic properties such as temperature, pressure and density for a fluid at rest are well defined for each fluid particle:

- *temperature* is the macroscopic measure of molecules (or atoms) kinetic energy and its unit of measure is Kelvin K;
- *density* is the macroscopic measure of the quantity of matter contained in a fluid particle and its unit of measure is Kg/m^3;
- *pressure* is the macroscopic measure of the force caused by the collision of molecules (or atoms) on a surface and its unit of measure is Pascal $Pa = N/m^2$. It is the same in each direction and it is normal to the surface on which it is applied.

All of the previous quantities are scalar fields. Another thermodynamic quantity that will be used later is the *internal energy* per mass unit e, which is defined from the *first principle of thermodynamic*: considering a closed system, the difference between the energy provided to the system as heat and the work done by the system on its surroundings is equal to the differece of internal energy of the system

$$\Delta e = q - w.$$

1 In ambient pressure air and $L = 1m$ we have $Kn = 6.8\,10^{-10}$

In a fluid at rest, all the fluid particles are in *thermodynamic equilibrium*.

For fluid in motion we define the velocity associated to a fluid particle $\boldsymbol{U}(t,\boldsymbol{x}) = d\boldsymbol{x}/dt$ as the mean constituent particles velocity within the fluid particle volume $\delta\Omega_p$ with respect to its centre of mass. It is a vector field with unit of measure m/s:

$$\boldsymbol{U}(t,\boldsymbol{x}) = \begin{bmatrix} U_1(t,\boldsymbol{x}) \\ U_2(t,\boldsymbol{x}) \\ U_3(t,\boldsymbol{x}) \end{bmatrix}$$

The *stress tensor* identifies the forces per area unit related to the molecular nature of the fluid. To identify the internal stresses at a point it is necessary to specify three stress components along three mutually orthogonal planes. The *stress tensor* is a symmetric second order tensor:

$$\boldsymbol{\sigma} = \begin{bmatrix} \sigma_{11} & \sigma_{12} & \sigma_{13} \\ \sigma_{21} & \sigma_{22} & \sigma_{23} \\ \sigma_{31} & \sigma_{23} & \sigma_{33} \end{bmatrix}.$$

The generic component σ_{ij} is the force per surface unit that acts in the plan with normal unit vector in the direction i and in the direction j. It contains both the thermodynamic pressure and the *shear stress tensor*:

$$\begin{bmatrix} \sigma_{11} & \sigma_{12} & \sigma_{13} \\ \sigma_{21} & \sigma_{22} & \sigma_{23} \\ \sigma_{31} & \sigma_{23} & \sigma_{33} \end{bmatrix} = \begin{bmatrix} -p & 0 & 0 \\ 0 & -p & 0 \\ 0 & 0 & -p \end{bmatrix} + \begin{bmatrix} \tau_{11} & \tau_{12} & \tau_{13} \\ \tau_{21} & \tau_{22} & \tau_{23} \\ \tau_{31} & \tau_{23} & \tau_{33} \end{bmatrix}.$$

The expression for the generic component of the shear stress tensor is:

$$\tau_{ij} = \mu \left(\frac{\partial U_i}{\partial x_j} + \frac{\partial U_j}{\partial x_i} \right) + \lambda \delta_{ij} \frac{\partial U_k}{\partial x_k};$$

this linear expression is valid just for *Newtonian fluids* and it is a second order symmetric tensor. It is attributable just to the motion of the fluid: in a fluid at rest $\boldsymbol{\tau}$ is a zero matrix. More precisely, $\boldsymbol{\tau}$ is related to the *strain rate tensor* $\boldsymbol{S}$, which is the symmetric part of the tensor $(\nabla \boldsymbol{U})_{ij} = \partial U_i / \partial x_j$:

$$\boldsymbol{S} = \frac{1}{2}(\nabla \boldsymbol{U} + \nabla \boldsymbol{U}^T) \quad S_{ij} = \frac{1}{2} \left(\frac{\partial U_i}{\partial x_j} + \frac{\partial U_j}{\partial x_i} \right),$$

such that $\tau_{ij} = 2\mu S_{ij} + \lambda S_{kk}\delta_{ij}$. The antisymmetric part of $\nabla \boldsymbol{U}$ is the *spin tensor*:

$$\Omega_{ij} = \frac{1}{2}\left(\frac{\partial U_i}{\partial x_j} - \frac{\partial U_j}{\partial x_i}\right).$$

The origin of this forces is attributable to the momentum diffusion due to the thermal agitation of adjacent constituent particles: the thermal agitation leads to a mutual exchange of constituent particles with different mean momentum. In a macroscopic context this behavior is summarized in the *viscosity coefficient* μ and in the *volume viscosity coefficient* λ with unit of measurement $Kg/(ms)$.

Defining the *pressure for the fluid in motion* p^* as

$$p^* = -\frac{1}{3}(\sigma_{11} + \sigma_{22} + \sigma_{33}),$$

we can write

$$p^* = p - \left(\lambda + \frac{2}{3}\mu\right)\nabla \cdot \boldsymbol{U}.$$

The charateristic time of the thermodynamic equilibrium achievement is way smaller than the characteristic time of most fluid flows that occur in pratical cases, so we can extend the definition of thermodynamic properties above at the case of fluid in motion. In this case, p^* is equal to the thermodynamic pressure p and this hypothesis leads to the *Stokes hypotesis* for λ, that is $\lambda = -(2/3)\mu$ and

$$\tau_{ij} = \mu\left(\frac{\partial U_i}{\partial x_j} + \frac{\partial U_j}{\partial x_i}\right) - \frac{2}{3}\mu\delta_{ij}\frac{\partial U_k}{\partial x_k}. \tag{1}$$

Based on the same mechanism of the viscosity momentum exchange, $\boldsymbol{q}$ is the heat flux $[W/m^2]$ due to a heat exchange from a warmer zone to a colder one; it stands the *Fourier law*:

$$\boldsymbol{q} = -k\nabla T$$

where k is the thermal conductivity coefficient an its unit of measure is $W/(mK)$.

1.2 NAVIER STOKES EQUATIONS

We can write the equations considering a control volume of the fluid, fixed in space, with the fluid moving through it. The fun-

damental physical principles that come into play in conventional fluid dynamics problems are:

- conservation of mass, which states that mass can't be created or destroyed;
- momentum balance, which states the net force applied is equal to the time rate of change of the momentum (*Newton's second law*);
- conservation of energy, based on the *first law of thermodynamics*.

The equations that arise from these principles applied to an infinitesimal control volume are the *Navier Stokes equations*. We report them in their differential form:

$$\begin{cases} \dfrac{\partial \rho}{\partial t} + \nabla \cdot (\rho \boldsymbol{U}) = 0 \\ \dfrac{\partial (\rho \boldsymbol{U})}{\partial t} + \nabla \cdot (\rho \boldsymbol{U}\boldsymbol{U}) = -\nabla p + \nabla \cdot \boldsymbol{\tau} + \rho \boldsymbol{f} \\ \dfrac{\partial E}{\partial t} + \nabla \cdot (E\boldsymbol{U}) = -\nabla \cdot (p\boldsymbol{U}) + \nabla \cdot (\boldsymbol{\tau} \cdot \boldsymbol{U}) + \rho \boldsymbol{f} \cdot \boldsymbol{U} - \nabla \cdot \boldsymbol{q} + Q_v, \end{cases} \tag{2}$$

where we used the conventions:

$$\nabla \cdot (\rho \boldsymbol{U}\boldsymbol{U}) = \begin{bmatrix} \nabla \cdot (\rho U_1 \boldsymbol{U}) \\ \nabla \cdot (\rho U_2 \boldsymbol{U}) \\ \nabla \cdot (\rho U_3 \boldsymbol{U}) \end{bmatrix}$$

and

$$\nabla \cdot \boldsymbol{\tau} = \begin{bmatrix} \dfrac{\partial \tau_{11}}{\partial x_1} & \dfrac{\partial \tau_{12}}{\partial x_2} & \dfrac{\partial \tau_{13}}{\partial x_3} \\ \dfrac{\partial \tau_{21}}{\partial x_1} & \dfrac{\partial \tau_{22}}{\partial x_2} & \dfrac{\partial \tau_{23}}{\partial x_3} \\ \dfrac{\partial \tau_{31}}{\partial x_1} & \dfrac{\partial \tau_{23}}{\partial x_2} & \dfrac{\partial \tau_{33}}{\partial x_3} \end{bmatrix}.$$

In the previous set of equations:

- $E = \rho(e + V^2/2)$ is the *total energy* per volume unit $[J/m^3]$, sum of the internal energy per volume unit and the kinetic energy per volume unit;

- Q_v is the term relating the possible presence of volumetric heat sources;
- $\rho \boldsymbol{f}$ is a generic force field per volume unit applied; for example an electromagnetic field or a gravitational field.

In classical aerodynamics theory volumetric heat sources are absent, while the force field per volume unit commonly applied is the gravitational field $\rho \boldsymbol{g}$, which can be usually neglected except for natural convection problems.

1.2.1 Closure of the problem

In the Navier-Stokes differential system (2) the following variables appear: $\rho, \boldsymbol{U}, p, T, E, \boldsymbol{\tau}, \boldsymbol{q}$; indeed, we already presented a constitutive equation for $\boldsymbol{\tau}$ and $\boldsymbol{q}$, so the number of the unknown variables is seven and the number of equation is five.

From now on we will consider just gases, in particular we are interested in air, and we get the missing equations from the *kinetic theory of gases*. The hypotesys beetween the kinetic theory of ideal gases are:

- an ideal gas consists of equal constituent particles in a continuous and chaotic motion;
- all the collisions are elastic;
- there aren't interactions forces between constituent particles, except during collisions [2].

For an *ideal gas* it stands the *ideal gas law*:

$$\frac{p}{\rho} = \frac{R}{M} T$$

where

- $R = 8314\, J/(Mole\, K)$ is the *universal gas constant*;
- M is the molar mass ($M = 28.96\, kg/Mole$ for the air);

2 In normal conditions fluid molecules are well spaced and intermolecular forces are negligible because they decay very quickly with distance.

Moreover, considering $e = 0\,J/kg$ at $T = 0\,K$, the internal energy per mass unit for a *calorically perfect gas* [3] can be calculated from

$$e = c_v T$$

where c_v is the specific heat capacity at constant volume. For the air:

$$c_v = \frac{R/M}{\gamma - 1} = 717.5\,\frac{J}{kg\,K}.$$

1.2.2 Incompressible condition

We can define the *Mach number*:

$$M = \frac{U}{a} = \frac{U}{\sqrt{\gamma RT}},$$

which is related to the compressibility effects that occur in the fluid in motion with characteristic velocity U. If $M < 0.4$, the compressibility effects are approximately negligible and the gas can be considered incompressible. This means that the density ρ is constant and the Navier Stokes equations become, without of volumetric heat sources and in absence of force field per volume unit applied,

$$\begin{cases} \nabla \cdot \boldsymbol{U} = 0 \\ \rho \dfrac{\partial \boldsymbol{U}}{\partial t} + \rho \boldsymbol{U} \cdot \nabla \boldsymbol{U} = -\nabla p + \nabla \cdot \boldsymbol{\tau}. \end{cases} \tag{3}$$

Expliciting them in the three direction we obtain:

$$\begin{cases} \dfrac{\partial U_1}{\partial x_1} + \dfrac{\partial U_2}{\partial x_2} + \dfrac{\partial U_3}{\partial x_3} = 0 \\ \rho \dfrac{\partial U_1}{\partial t} + \rho \nabla \cdot (U_1 \boldsymbol{U}) = -\dfrac{\partial p}{\partial x_1} + \dfrac{\partial \tau_{11}}{\partial x_1} + \dfrac{\partial \tau_{12}}{\partial x_2} + \dfrac{\partial \tau_{13}}{\partial x_3} \\ \rho \dfrac{\partial U_2}{\partial t} + \rho \nabla \cdot (U_2 \boldsymbol{U}) = -\dfrac{\partial p}{\partial x_2} + \dfrac{\partial \tau_{21}}{\partial x_1} + \dfrac{\partial \tau_{22}}{\partial x_2} + \dfrac{\partial \tau_{23}}{\partial x_3} \\ \rho \dfrac{\partial U_3}{\partial t} + \rho \nabla \cdot (U_3 \boldsymbol{U}) = -\dfrac{\partial p}{\partial x_3} + \dfrac{\partial \tau_{31}}{\partial x_1} + \dfrac{\partial \tau_{32}}{\partial x_2} + \dfrac{\partial \tau_{33}}{\partial x_3} \end{cases}$$

3 In a calorically perfect gas c_v and c_p are constant and they aren't temperature dependent. This is true for T below $1000\,K$ in atmospheric pressure; than the vibrational motion of molecules becomes important and c_v and c_p vary with T. An ideal gas is also calorically perfect.

We don't consider the energy equation anymore because in this situation the energy equation is decoupled from the others and it can be resolved subsequently. Since the divergence of $\boldsymbol{U}$ is zero, the stress tensor is simplified:

$$\tau_{ij} = \mu\left(\frac{\partial U_i}{\partial x_j} + \frac{\partial U_j}{\partial x_i}\right) - \frac{2}{3}\mu\delta_{ij}\frac{\partial U_k}{\partial x_k} = \mu\left(\frac{\partial U_i}{\partial x_j} + \frac{\partial U_j}{\partial x_i}\right),$$

moreover

$$\begin{aligned}
&\frac{\partial \tau_{11}}{\partial x_1} + \frac{\partial \tau_{12}}{\partial x_2} + \frac{\partial \tau_{13}}{\partial x_3} = \\
&= 2\mu\frac{\partial^2 U_1}{\partial x_1^2} + \mu\frac{\partial}{\partial x_2}\left(\frac{\partial U_1}{\partial x_2} + \mu\frac{\partial U_2}{\partial x_1}\right) + \mu\frac{\partial}{\partial x_3}\left(\frac{\partial U_1}{\partial x_3} + \mu\frac{\partial U_3}{\partial x_1}\right) = \\
&= 2\mu\frac{\partial^2 U_1}{\partial x_1^2} + \mu\frac{\partial^2 U_1}{\partial x_2^2} + \mu\frac{\partial^2 U_1}{\partial x_3^2} + \mu\frac{\partial}{\partial x_1}\frac{\partial U_2}{\partial x_2} + \mu\frac{\partial}{\partial x_1}\frac{\partial U_3}{\partial x_3} = \\
&= \mu\triangle U_1 + \mu\frac{\partial}{\partial x_1}\left(\frac{\partial U_1}{\partial x_1} + \frac{\partial U_2}{\partial x_2} + \frac{\partial U_3}{\partial x_3}\right) = \mu\triangle U_1.
\end{aligned}$$

Similarly:

$$\begin{aligned}
\frac{\partial \tau_{21}}{\partial x_1} + \frac{\partial \tau_{22}}{\partial x_2} + \frac{\partial \tau_{23}}{\partial x_3} &= \mu\triangle U_2, \\
\frac{\partial \tau_{31}}{\partial x_1} + \frac{\partial \tau_{32}}{\partial x_2} + \frac{\partial \tau_{33}}{\partial x_3} &= \mu\triangle U_3.
\end{aligned}$$

So, the equations became

$$\begin{cases}
\dfrac{\partial U_1}{\partial x_1} + \dfrac{\partial U_2}{\partial x_2} + \dfrac{\partial U_3}{\partial x_3} = 0 \\
\rho\dfrac{\partial U_1}{\partial t} + \rho\nabla\cdot(U_1\boldsymbol{U}) = -\dfrac{\partial p}{\partial x_1} + \mu\triangle U_1 \\
\rho\dfrac{\partial U_2}{\partial t} + \rho\nabla\cdot(U_2\boldsymbol{U}) = -\dfrac{\partial p}{\partial x_2} + \mu\triangle U_2 \\
\rho\dfrac{\partial U_3}{\partial t} + \rho\nabla\cdot(U_3\boldsymbol{U}) = -\dfrac{\partial p}{\partial x_3} + \mu\triangle U_3.
\end{cases}$$

The system of Navier Stokes equations for an incompressible flow consists in four unknown variables, which are the three components of $\boldsymbol{U}$ and p, and four equation, which are the mass conservation equation and the momentum equations in the three direction.

In *Einstein notation*[4] the Navier Stokes equations become:

$$\begin{cases} \dfrac{\partial U_i}{\partial x_i} = 0 \\ \rho \dfrac{\partial U_j}{\partial t} + \rho \dfrac{\partial U_i U_j}{\partial x_i} = -\dfrac{\partial p}{\partial x_j} + \mu \dfrac{\partial^2 U_j}{\partial x_i \partial x_i}. \end{cases} \tag{4}$$

We note that

$$\frac{\partial U_i U_j}{\partial x_i} = U_i \frac{\partial U_j}{\partial x_i} + U_j \frac{\partial U_i}{\partial x_i} = U_i \frac{\partial U_j}{\partial x_i}.$$

In incompressible flows pressure in not related to ρ anymore, it loses its thermodynamic role and lends itself to a new interpretation.

The *Poisson equation* for the pressure is obatined adding the momentum equation in x direction derived with respect to x, the momentum equation in y direction derived with respect to y and the momentum equation in z direction derived with respect to z. All the terms containing the divergence of $\boldsymbol{U}$ are zero, and the resulting equation will be:

$$\frac{\partial^2 p}{\partial x_i \partial x_i} = -\rho \frac{\partial}{\partial x_j} \left(U_i \frac{\partial U_j}{\partial x_i} \right) = -\rho \frac{\partial U_i}{\partial x_j} \frac{\partial U_j}{\partial x_i}.$$

The *Poisson equation* is a necessary and sufficient condition to satisfy the solenoidal condition on velocity field.

1.2.3 Non-dimensional equations and Reynolds number

The most important parameter in fluid dynamics is the *Reynolds number*

$$Re = \frac{U \rho L}{\mu} = \frac{UL}{\nu}$$

where L represents a characteristic dimension of the flow. It is proportional to the ratio of inertial forces to viscous forces. At low Reynolds number the action of viscous forces is sufficient to damp velocity perturbations and the flow appears smooth: this is called a *laminar flow*. A flow characterized by a high Reynolds

4 This notation implies summation when an index appears twice in a term.

number, otherwise, is intrinsically unstable, unsteady, produces turbulent structures named *eddies* and it is called *turbulent flow*.

The Reynolds number is the only parameter that appears in the non-dimensional Navier Stokes equations for incompressible flows. Considering a fluid dynamics experiment characterized by a *length scale* L, a *velocity scale* U and a *time scale* U/L, we define non-dimensional indipendent variables as

$$\hat{\boldsymbol{x}} = \frac{\boldsymbol{x}}{L}$$

$$\hat{t} = \frac{t}{U/L},$$

and non dimensional dependent variables as:

$$\hat{\boldsymbol{U}}(\hat{\boldsymbol{x}}, \hat{t}) = \frac{\boldsymbol{U}(\boldsymbol{x}, t)}{U}$$

$$\hat{p}(\hat{\boldsymbol{x}}, \hat{t}) = \frac{p(\boldsymbol{x}, t)}{\rho U^2}.$$

The non dimensional Navier Stokes equations are:

$$\begin{cases} \dfrac{\partial \hat{U}_i}{\partial \hat{x}_i} = 0 \\ \dfrac{\partial \hat{U}_j}{\partial \hat{t}} + \hat{U}_i \dfrac{\partial \hat{U}_j}{\partial \hat{x}_i} = -\dfrac{\partial \hat{p}}{\partial \hat{x}_j} + \dfrac{1}{Re} \dfrac{\partial^2 \hat{U}_j}{\partial \hat{x}_i \partial \hat{x}_i}, \end{cases} \tag{5}$$

while the non dimensional Poisson equation is:

$$\frac{\partial^2 \hat{p}}{\partial \hat{x}_i \partial \hat{x}_i} = -\frac{\partial}{\partial \hat{x}_j} \left(\hat{U}_i \frac{\partial \hat{U}_j}{\partial \hat{x}_i} \right) = -\frac{\partial \hat{U}_i}{\partial \hat{x}_j} \frac{\partial \hat{U}_j}{\partial \hat{x}_i}.$$

An important property of the equations is the *Reynolds number similarity*. Considering two experiments a and b with:

- geometrically similar domains, differing just by a scale factor,
- different length scale L_a and L_b,
- different velocity scale U_a and U_b,
- different fluid properties ν_a and ν_b,

- same Reynolds number, such that $Re_a = U_a L_a/\nu_a = Re_b = U_b L_b/\nu_b$,
- same non dimensional boundary conditions,

the two experiments are governed by the same equations and the results $\hat{\boldsymbol{U}}$ and $\hat{p}$ will be the same. A significant point in this thesis is that the *non-dimensional Navier Stokes equations for incompressible flows, once the domain and the boundary conditions are fixed, depend just by one parameter, which is the Reynolds number.*

1.3 SOME TURBULENCE MODELLING

Turbulence modelling consists in a mix of theoretical and empirical approaches and it's still an open field. For this reason, we are not going to cover all the details but we are just interested in the main ideas and equations that will be used in the simulations executed further on this thesis. The models presented are just a reference and they vary depending on the computational fluid dynamics software used. A summary of *RANS* turbulence models is provided in [NASA resource], that takes as reference relevant papers such as [Chien] and [Wilcox-1].

1.3.1 Turbulent boundary layer

Turbulent flow boundary layer is divided into two parts: the *inner layer* and the *outer layer*. In the inner layer exists a universal self similar solution for the mean velocity parallel to the wall as a function of the distance from the wall if these two variables are appropriately scaled. We introduce some definitions:

- τ_w is the *wall shear stress*,
- $u_\tau = \sqrt{\frac{\tau_w}{\rho}}$ is the *friction velocity*,
- $u^+ = \frac{u}{u_\tau}$ is the dimensionless velocity parallel to the wall,
- $y^+ = \frac{y u_\tau}{\nu}$ is the dimensionless distance from the wall,

It stands the *law of the wall*, valid for $30 < y^+ < 200$ (*log-law region*)

$$u^+ = \frac{1}{K} ln(y^+) + C,$$

where

- $K = 0.41$ is the *von Kármán* constant,
- $C = 5$ if the wall is smooth.

Below this region there are the *buffer layer*, that extends for $5 < y^+ < 30$, and the *inner layer*, for value of y^+ below 5. In the inner layer $u^+ = y^+$, while the buffer layer is a fitting region from the inner layer and the log-law region and no analytic expression exists.

In fluid dinamycs turbulent flow simulations it is important to have the first layer of cells in the inner layer, if we want to catch all the boundary layer, or in the log-law region, where the trend of the velocity is known and we can use *near-wall treatment* methods implemented in *CFD* software. It should be noted that we don't know the value of τ_w a priori, so an estimate or a test simulation is needed.

Anyway, a single formula that represents the boundary layer in its entirety, with good results, is proposed by [Spalding]:

$$\begin{aligned} y^+ = u^+ + 0.1108[e^{0.4u^+} - 1 - 0.4u^+ - (0.4u^+)^2/2! + \\ - (0.4u^+)^3/3! - (0.4u^+)^4/4!. \end{aligned} \tag{6}$$

1.3.2 Mean flow equations

In order to get the mean flow equations, in 1894 Reynolds introduced the following decomposition of the velocity:

$$\boldsymbol{U}(\boldsymbol{x}, t) = \langle \boldsymbol{U}(\boldsymbol{x}, t) \rangle + \boldsymbol{u}(\boldsymbol{x}, t),$$

where $\langle \boldsymbol{U}(\boldsymbol{x}, t) \rangle$ is the time average of $\boldsymbol{U}(\boldsymbol{x}, t)$ and $\boldsymbol{u}(\boldsymbol{x}, t)$ it is the fluctuation term. We can apply this decomposition to the *Navier Stokes* equations (4):

$$\begin{cases} \dfrac{\partial U_i}{\partial x_i} = 0 \\ \rho \dfrac{\partial U_j}{\partial t} + \rho \dfrac{\partial U_i U_j}{\partial x_i} = -\dfrac{\partial p}{\partial x_j} + \mu \dfrac{\partial^2 U_j}{\partial x_i \partial x_i} \end{cases}$$

The mean and the differentiation commute. Averaging the continuity equation, we obtain

$$\left\langle \frac{\partial U_i}{\partial x_i} \right\rangle = \frac{\partial \langle U_i \rangle}{\partial x_i} = 0$$

moreover

$$\frac{\partial U_i}{\partial x_i} = \frac{\partial \left(\langle U_i \rangle + u_i \right)}{\partial x_i} = \frac{\partial u_i}{\partial x_i} = 0.$$

so $\langle \boldsymbol{U}(\boldsymbol{x}, t) \rangle$ and $\boldsymbol{u}(\boldsymbol{x}, t)$ are both solenoidal. Now we have to average the momentum equation:

$$\rho \left\langle \frac{\partial U_j}{\partial t} \right\rangle + \rho \left\langle \frac{\partial U_i U_j}{\partial x_i} \right\rangle = - \left\langle \frac{\partial p}{\partial x_j} \right\rangle + \mu \left\langle \frac{\partial^2 U_j}{\partial x_i \partial x_i} \right\rangle$$

$$\rho \frac{\partial \langle U_j \rangle}{\partial t} + \rho \frac{\partial \langle U_i U_j \rangle}{\partial x_i} = - \frac{\partial \langle p \rangle}{\partial x_j} + \mu \frac{\partial^2 \langle U_j \rangle}{\partial x_i \partial x_i}.$$

We note that:

$$U_i U_j = (\langle U_i \rangle + u_i)(\langle U_j \rangle + u_j) = \langle U_i \rangle \langle U_j \rangle + \langle U_i \rangle u_j + u_i \langle U_j \rangle + u_i u_j$$

- $\langle \langle U_i \rangle \langle U_j \rangle \rangle = \langle U_i \rangle \langle U_j \rangle$,
- $\langle u_i \rangle = \langle U_i - \langle U_i \rangle \rangle = \langle U_i \rangle - \langle U_i \rangle = 0$
- $\langle \langle U_i \rangle u_j \rangle = \langle U_i \rangle \langle u_j \rangle = 0$,
- $\langle u_i \langle U_j \rangle \rangle = \langle U_j \rangle \langle u_i \rangle = 0$,

Then,

$$\langle U_i U_j \rangle = \langle U_i \rangle \langle U_j \rangle + \langle u_i u_j \rangle$$

and the momentum equation becomes

$$\rho \frac{\partial \langle U_j \rangle}{\partial t} + \rho \langle U_i \rangle \frac{\partial \langle U_j \rangle}{\partial x_i} = - \frac{\partial \langle p \rangle}{\partial x_j} + \mu \frac{\partial^2 \langle U_j \rangle}{\partial x_i \partial x_i} - \rho \frac{\partial \langle u_i u_j \rangle}{\partial x_i},$$

which can also be written as

$$\rho \frac{\partial \langle U_j \rangle}{\partial t} + \rho \langle U_i \rangle \frac{\partial \langle U_j \rangle}{\partial x_i} = - \frac{\partial \langle p \rangle}{\partial x_j} + \mu \frac{\partial}{\partial x_i} \left[\frac{\partial \langle U_j \rangle}{\partial x_i} + \frac{\partial \langle U_i \rangle}{\partial x_j} - \rho \langle u_i u_j \rangle \right]. \tag{7}$$

while the *Poisson equation* for the mean pressure is:

$$\frac{\partial^2 \langle p \rangle}{\partial x_i \partial x_j} = -\rho \frac{\partial \langle U_i \rangle}{\partial x_j} \frac{\partial \langle U_j \rangle}{\partial x_i} - \rho \frac{\partial^2 \langle u_i u_j \rangle}{\partial x_i \partial x_j}.$$

The resulting system of equations is the *Reynolds averaged Navier Stokes* (RANS) system:

$$\begin{cases} \dfrac{\partial \langle U_i \rangle}{\partial x_i} = 0 \\ \rho \dfrac{\partial \langle U_j \rangle}{\partial t} + \rho \langle U_i \rangle \dfrac{\partial \langle U_j \rangle}{\partial x_i} = -\dfrac{\partial \langle p \rangle}{\partial x_j} + \mu \dfrac{\partial^2 \langle U_j \rangle}{\partial x_i \partial x_i} - \rho \dfrac{\partial \langle u_i u_j \rangle}{\partial x_i}. \end{cases} \tag{8}$$

The term $-\rho \langle u_i u_j \rangle$ is the *Reynolds stress tensor* and it represents the momentum transfer due to the velocity fluctuations. It is a simmetric second order tensor. We don't have information about the fluctuation field and because of that it needs to be modelled somehow.

The *turbulent kinetic energy* is defined as:

$$k(\boldsymbol{x}, t) = \frac{1}{2} \langle u_i u_i \rangle$$

and it is half the trace of the tensor $\langle u_i u_j \rangle$.

1.3.3 Turbulent viscosity model

The *turbulent viscosity hypothesis* is one of the most common way to proceed and it consists in modelling the deviatoric Reynolds stress as the shear stress tensor (1):

$$-\rho \langle u_i u_j \rangle + \frac{2}{3} \rho k \delta_{ij} = \mu_t \left(\frac{\partial \langle U_i \rangle}{\partial x_j} + \frac{\partial \langle U_j \rangle}{\partial x_i} \right) - \frac{2}{3} \mu_t \delta_{ij} \frac{\partial \langle U_k \rangle}{\partial x_k}. \tag{9}$$

Equation (7) becomes

$$\rho \frac{\partial \langle U_j \rangle}{\partial t} + \rho \langle U_i \rangle \frac{\partial \langle U_j \rangle}{\partial x_i} = -\frac{\partial \langle p \rangle}{\partial x_j} +$$
$$+ \frac{\partial}{\partial x_i} \left[\mu_{eff} \left(\frac{\partial \langle U_i \rangle}{\partial x_j} + \frac{\partial \langle U_j \rangle}{\partial x_i} \right) - \frac{2}{3} \mu_t \delta_{ij} \frac{\partial \langle U_k \rangle}{\partial x_k} \right] - \rho \delta_{ij} \frac{2}{3} \frac{\partial k}{\partial x_i}$$

and, remembering that $\langle \boldsymbol{U} \rangle$ is solenoidal,

$$\rho \frac{\partial \langle U_j \rangle}{\partial t} + \rho \langle U_i \rangle \frac{\partial \langle U_j \rangle}{\partial x_i} = -\frac{\partial}{\partial x_j}\left(\langle p \rangle + \frac{2}{3}\rho k \right) + \\ + \frac{\partial}{\partial x_i}\left[\mu_{eff} \left(\frac{\partial \langle U_j \rangle}{\partial x_i} + \frac{\partial \langle U_i \rangle}{\partial x_j} \right) \right],$$

with

$$\mu_{eff}(\boldsymbol{x}, t) = \mu_t(\boldsymbol{x}, t) + \mu = \rho(\nu_t(\boldsymbol{x}, t) + \nu).$$

We need now an expression for $\nu_t(\boldsymbol{x}, t)$ in order to close the system of equations. It can be seen as the product between a velocity and a length scale:

$$\nu_t = u^* l_m,$$

where l_m is the *mixing length*, a characteristic distance where a fluid particle conserve its properties, and u^* is a velocity scale (see next section).

1.3.4 Standard k - ϵ model

In this model we use k and ε to get the turbulent viscosity. ε is the *turbulent kinetic energy dissipation rate* and it is defined as:

$$\varepsilon = \nu \left\langle \frac{\partial u_i}{\partial x_j} \frac{\partial u_j}{\partial x_i} \right\rangle.$$

The velocity scale u^* can be based on turbulent kintic energy

$$u^* = c k^{1/2}$$

where c is a constant. On the other hand, ε scales as $(u^*)^3/l_m$ and a reasonable model is

$$\varepsilon = C_D \frac{k^{3/2}}{l_m},$$

where C_D is another constant. Finally

$$\nu_t = c k^{1/2} l_m = c k^{1/2} \frac{C_D k^{3/2}}{\varepsilon} = C_\mu \frac{k^2}{\varepsilon},$$

with C_μ usually taken as $C_\mu = 0.09$.

The *turbulent kinetic energy* and the *turbulent kinetic energy dissipation rate* are calculated from two scalar transport equation, derived from Navier Stokes equations and some empirical modelling. The equation for k is

$$\frac{\partial(\rho k)}{\partial t} + \frac{\partial}{\partial x_j}(\rho k \langle U_j \rangle) = \frac{\partial}{\partial x_j}\left[\left(\mu + \frac{\mu_t}{\sigma_k}\right)\frac{\partial k}{\partial x_j}\right] + P - \rho\varepsilon + \rho L_k, \tag{10}$$

while the equation for ε is

$$\frac{\partial(\rho\varepsilon)}{\partial t} + \frac{\partial}{\partial x_j}(\rho\varepsilon \langle U_j \rangle) = \frac{\partial}{\partial x_j}\left[\left(\mu + \frac{\mu_t}{\sigma_\varepsilon}\right)\frac{\partial \varepsilon}{\partial x_j}\right] + C_{1\varepsilon}\frac{\varepsilon}{k}P + \tag{11}$$

$$- C_{2\varepsilon} f \rho \frac{\varepsilon^2}{k} + \rho L_\varepsilon \tag{12}$$

where:

- $\frac{\partial}{\partial x_j}(\rho k \langle U_j \rangle)$ and $\frac{\partial}{\partial x_j}(\rho\varepsilon \langle U_j \rangle)$ are the convection terms,
- $\frac{\partial}{\partial x_j}\left[\left(\mu + \frac{\mu_t}{\sigma_k}\right)\frac{\partial k}{\partial x_j}\right]$ and $\frac{\partial}{\partial x_j}\left[\left(\mu + \frac{\mu_t}{\sigma_\varepsilon}\right)\frac{\partial \varepsilon}{\partial x_j}\right]$ are the diffusion terms,
- $P = -\rho \langle u_i u_j \rangle \frac{\partial \langle U_j \rangle}{\partial x_i}$ is the production term of k and it is modelled using equation (9),
- $C_{1\varepsilon}$, $C_{2\varepsilon}$, C_μ, σ_k, σ_ε, $C_{3\varepsilon}$ are model constants; suggested values are $C_{1\varepsilon} = 1.35$, $C_{2\varepsilon} = 1.80$, $C_\mu = 0.09$, $\sigma_k = 1.0$, $\sigma_\varepsilon = 1.3$, $C_{3\varepsilon} = -0.33$,
- $L_k = -2\frac{\mu k}{\rho d^2}$ and $L_\varepsilon = -2\frac{\mu\varepsilon}{\rho d^2}e^{-d^+/2}$ are internal source term for k and ε, where d is the minimum distance from the wall and $d^+ = d\rho u_\tau/\mu$,
- f is an auxiliary function $f = 1 - \frac{0.4}{1.8}e^{Re_T^2/36}$, where $Re_T = \frac{\rho k^2}{\mu\varepsilon}$.

To discuss initial and boundary conditions we consider a simpe *duct* where the flow is evolving from left to right. Inlet boundary

conditions for k an ε are estimated by relations for isotropic turbulence, in particular:

$$k = \frac{1}{2}\left(u_1^2 + u_2^2 + u_3^2\right) \simeq \frac{3}{2}(IU)^2 \tag{13}$$

$$\varepsilon = \frac{C_\mu^{0.75} k^{1.5}}{l}, \tag{14}$$

where

- U is a reference flow speed,
- I is the *turbulent intensity* (a common value is $I = 0.05$),
- l is the *turbulent length scale* and a reference value is $l = 0.07L$, where L is the characteristic length of the flow.

Natural boundary conditions at the wall are $k_{wall} = 0$ and $\varepsilon_{wall} = 0$, but with this model it is recommended to use *wall treatment* instead of resolving the boundary layer entirely. At the outlet, that ideally is far from the inlet, it is possible to use *zero gradient* conditions for k and ε.

1.3.5 The k - ω model

In the k-ω model, instead of using a transport equation for ε, a trasport equation for ω is used; ω is the *turbulent specific dissipation rate* and it is defined as:

$$\omega = \frac{\varepsilon}{C_\mu k} \quad [s^{-1}]$$

and the turbulent viscosity is computed slightly differently:

$$\nu_t = \frac{k}{\hat{\omega}},$$

with

$$\hat{\omega} = max\left[\omega, \frac{7}{8}\sqrt{\frac{2\overline{S_{ij}}\,\overline{S_{ij}}}{C_\mu}}\right], \quad \overline{S_{ij}} = S_{ij} - \frac{1}{3}\frac{\partial u_k}{\partial x_k}\delta_{ij}.$$

The relative transport equation is

$$\frac{\partial(\rho\omega)}{\partial t} + \frac{\partial}{\partial x_j}(\rho\omega \left\langle U_j \right\rangle) = \frac{\partial}{\partial x_j}\left[(\mu + \sigma_\omega \mu_t)\frac{\partial \omega}{\partial x_j}\right] + \gamma\frac{\omega}{k}P + \quad (15)$$

$$- \beta\rho\omega^2 + \frac{\rho\sigma_d}{\omega}\frac{\partial k}{\partial x_j}\frac{\partial \omega}{\partial x_j}. \quad (16)$$

while the transport equation used for k is

$$\frac{\partial(\rho k)}{\partial t} + \frac{\partial}{\partial x_j}(\rho k \left\langle U_j \right\rangle) = \frac{\partial}{\partial x_j}\left[(\mu + \sigma_k \mu_t)\frac{\partial k}{\partial x_j}\right] + P - C_\mu \rho k \omega. \quad (17)$$

where

- $\gamma = 13/25$, , $\sigma_k = 0.6$, $\sigma_\omega = 0.5$,
- $\beta = 0.0708\dfrac{1 + 85\chi_\omega}{1 + 100\chi_\omega}$,
- $\chi_\omega = \left|\dfrac{\Omega_{ij}\Omega_{jk}\hat{S}_{ki}}{(C_\mu\omega)^3}\right|$,
- $\hat{S}_{ij} = S_{ki} - \dfrac{1}{2}\dfrac{\partial u_m}{\partial x_m}\delta_{ki}$.

The inlet boundary condition for ω for isotropic turbulence is

$$\omega = \frac{k^{0.5}}{C_\mu^{0.25} l}, \quad (18)$$

while a recommended wall boundary condition is

$$\omega_{wall} = 10\frac{6\nu}{\beta_1 d^2}, \quad (19)$$

where d is the normal distance from the wall to the first cell centroid, $\beta_1 = 0.075$ and ν the freestream kinematic viscosity.

1.3.6 The k - ω SST model

The *k - ω shear stress transport* model combine the *k-ε* formulation, which works well in the free stream, and the *k-ω* model, which is prefered in the inner parts of the boundary layer. This is obtained

using a hyperbolic tangent *blending function* F_1 such that $F_1 = 1$ in the boundary layer and $F_1 = 0$ in the free stream:

$$\frac{\partial(\rho\omega)}{\partial t} + \frac{\partial}{\partial x_j}(\rho\omega \langle U_j \rangle) = \frac{\partial}{\partial x_j}\left[(\mu + \sigma_\omega \mu_t)\frac{\partial \omega}{\partial x_j}\right] + \frac{\gamma}{\nu_t}P + \quad (20)$$

$$- \beta\rho\omega^2 + 2(1 - F_1)\frac{\rho\sigma_{\omega 2}}{\omega}\frac{\partial k}{\partial x_j}\frac{\partial \omega}{\partial x_j}. \quad (21)$$

The general model constant ϕ is defined through the blending function F_1, an inner value ϕ_1 and an outer value ϕ_2:

$$\phi = F_1\phi_1 + (1 - F_1)\phi_2.$$

The standard model constants are:

- $\sigma_{k1} = 0.85$ and $\sigma_{k2} = 1$,
- $\sigma_{\omega_1} = 0.5$ and $\sigma_{\omega_2} = 0.876$,
- $\beta_1 = 0.075$ and $\beta_2 = 0.0828$,
- $\gamma_1 = \frac{\beta_1}{C_\mu} - \frac{\sigma_{\omega_1}\kappa^2}{\sqrt{C_\mu}}$, $\gamma_2 = \frac{\beta_2}{C_\mu} - \frac{\sigma_{\omega_2}\kappa^2}{\sqrt{C_\mu}}$ and $\kappa = 0.41$.

This model has a better performance in flow separation prediction and it is less sensitive to free stream conditions. Also in this case, the turbulent viscosity is calculated through a limiter function:

$$\nu_t = \frac{a_1 k}{max(a_1\omega, SF_2)}$$

where F_2 is a second blending function, a_1 is a constant with default value $a_1 = 0.31$ and S is the *strain rate magnitude* and it is defined as $S = \sqrt{2\boldsymbol{S} : \boldsymbol{S}}$, where $(\boldsymbol{S} : \boldsymbol{S})$ stands for $\sum_i \sum_j S_{ij}$.

To summarize, the equations to be solved are:

$$\frac{\partial \langle U_i \rangle}{\partial x_i} = 0$$

$$\rho\frac{\partial \langle U_j \rangle}{\partial t} + \rho \langle U_i \rangle \frac{\partial \langle U_j \rangle}{\partial x_i} = -\frac{\partial}{\partial x_j}\left(\langle p \rangle + \frac{2}{3}\rho k\right) + \\ + \frac{\partial}{\partial x_i}\left[\rho(\nu_t + \nu)\left(\frac{\partial \langle U_j \rangle}{\partial x_i} + \frac{\partial \langle U_i \rangle}{\partial x_j}\right)\right],$$

with ν_t obtained as reported in Table 1.

RANS models summary	
Model	k-ε
Auxiliary transport equations	(10) and (11)
ν_t	$C_\mu k^2/\varepsilon$
Auxiliary funtions	$f = 1 - 0.4e^{Re_T^2/36}/1.8$ $Re_T = \frac{\rho k^2}{\mu\varepsilon}$
Model coefficients	$C_\mu = 0.09$ $C_{1\varepsilon} = 1.35$ $C_{2\varepsilon} = 1.80$ $\sigma_k = 1.0$ $\sigma_\varepsilon = 1.3$ $C_{3\varepsilon} = -0.33$
Model	k-ω
Auxiliary transport equations	(17) and (15)
ν_t	$k/\hat{w}$ $\hat{\omega} = max\left[\omega, \frac{7}{8}\sqrt{\frac{2\overline{S_{ij}}\,\overline{S_{ij}}}{C_\mu}}\right]$ $\overline{S_{ij}} = S_{ij} - \frac{1}{3}\frac{\partial u_k}{\partial x_k}\delta_{ij}$
Model coefficients	$\gamma = 13/25$ $\sigma_k = 0.6$ $\sigma_\omega = 0.5$ $\beta = 0.0708\frac{1+85\chi_\omega}{1+100\chi_\omega}$ $\chi_\omega = \left\lvert\frac{\Omega_{ij}\Omega_{jk}\hat{S}_{ki}}{(C_\mu\omega)^3}\right\rvert$

Table 1

Model	k-ω SST
Auxiliary transport equations	(17) and (20)
ν_t	$a_1 k / max(a_1\omega, SF_2)$ $a_1 = 0.31$ $S = \sqrt{2\boldsymbol{S} : \boldsymbol{S}}$
Auxiliary funtions	F_1, F_2 blending functions
General model coefficient	$\phi = F_1\phi_1 + (1 - F_1)\phi_2$
Model coefficients	$\sigma_{k1} = 0.85$ $\sigma_{k2} = 1$ $\sigma_{\omega_1} = 0.5$ $\sigma_{\omega_2} = 0.876$ $\beta_1 = 0.075$ $\beta_2 = 0.0828$ $\kappa = 0.41$ $\gamma_1 = \frac{\beta_1}{C_\mu} - \frac{\sigma_{\omega_1}\kappa^2}{\sqrt{C_\mu}}$ $\gamma_2 = \frac{\beta_2}{C_\mu} - \frac{\sigma_{\omega_2}\kappa^2}{\sqrt{C_\mu}}$

1.3.7 Large eddy simulations

As we said, turbulent flows are characterized by the presence of coherent swirling structures named *eddies*. The largest eddies arise from the mean flow and they have the same dimension of the characteristic length of the flow, their Reynolds number is high and inertial forces are predominant. These big eddies are unstable, they break down generating smaller eddies in a process that is approximately dissipation free. This mechanism, called *energy cascade*, keeps going until the Reynolds number of the eddies are so low that the molecular diffusion is strong enough to dissipate into heat all the turbulent kinetic energy. This happens at the *Kolmogorov scale* η when the Reynolds number of the eddies is $Re_\eta \simeq 1$. The Kolmogorov scale is the mean minimun dimension of the eddies that we can expect in a turbulent flow and it can be estimated as:

$$\eta = \left(\frac{\nu^3}{\varepsilon}\right)^{1/4}.$$

To detect the smallest eddies at least four cells with side $d = \eta/2$ are necessary. The computational cost to resolve all these scales reveals too high and the aim of a large eddy simulation is to resolve just a part of the energy spectrum and model the smaller turbulent scales. This is obtained through a *low-pass filtering* operation on the Navier Stokes equations. The velocity is decomposed in a filtered velocity $\overline{\boldsymbol{U}}(\boldsymbol{x}, t)$ and in a subgrid scale velocity $\boldsymbol{u}'(\boldsymbol{x}, t)$:

$$\boldsymbol{U}(\boldsymbol{x}, t) = \overline{\boldsymbol{U}}(\boldsymbol{x}, t) + \boldsymbol{u}'(\boldsymbol{x}, t),$$

where the general filetring operator is a convolution over all the flow domain:

$$\overline{\boldsymbol{U}}(\boldsymbol{x}, t) = \int G(\boldsymbol{r}, \boldsymbol{x})\boldsymbol{U}(\boldsymbol{x} - \boldsymbol{r}, t)d\boldsymbol{r}, \tag{22}$$

with $\int G(\boldsymbol{r}, \boldsymbol{x})d\boldsymbol{r} = 1$. A filter characteristic is the filter width in the i direction Δ_i, which is a function of the grid scale and it defines the *subgrid length scale*, which is the scale that divides the resolved scales and the modelled scales. In the simplest case, it

can be the cube root of the cell volume. A simple example of filter is

$$G(\boldsymbol{r}) = \prod_{i=1}^{3} \frac{1}{\Delta_i} H\left(\frac{\Delta_i}{2} - |r_i|\right)$$

where H is the *Heaviside* function and Δ_i is the grid spacing in the direction i. The resulting filtered velocity is, for a cell centered in $\boldsymbol{x} = (x_1, x_2, x_3)$,

$$\overline{\boldsymbol{U}}(\boldsymbol{x}, t) = \frac{1}{\Delta_1 \Delta_2 \Delta_3} \int_{x_3-\Delta_3/2}^{x_3+\Delta_3/2} \int_{x_2-\Delta_2/2}^{x_2+\Delta_2/2} \int_{x_1-\Delta_1/2}^{x_1+\Delta_1/2} \boldsymbol{U}(\boldsymbol{x}', t) dx_1' dx_2' dx_3'$$

which is the mean velocity in the cell. The equation for the filtered velocity and the filtered pressure are obtained applying the filtering operator on the system of equations (4):

$$\begin{cases} \dfrac{\partial \overline{U}_i}{\partial x_i} = 0 \\ \rho \dfrac{\partial \overline{U}_j}{\partial t} + \rho \dfrac{\partial \overline{U_i U_j}}{\partial x_i} = -\dfrac{\partial \overline{p}}{\partial x_j} + \mu \dfrac{\partial^2 \overline{U}_j}{\partial x_i \partial x_i}. \end{cases}$$

As we have done with the Reynolds stress tensor, which is $\langle u_i u_j \rangle = \langle U_i \rangle \langle U_j \rangle - \langle U_i U_j \rangle$, we introduce now the *residual stress tensor* τ_{ij}^R, defined as:

$$\tau_{ij}^R = \overline{U_i U_j} - \overline{U_i}\,\overline{U_j},$$

the *subgrid scale kinetic energy* $k_{sgs} = \tau_{ii}^R/2$ and the *anisotropic residual stress tensor*

$$\tau_{ij}^r = \tau_{ij}^R - \frac{2}{3} k_{sgs} \delta_{ij}.$$

The momentum equation can be written as:

$$\rho \frac{\partial \overline{U}_j}{\partial t} + \rho \frac{\partial \overline{U_i}\,\overline{U_j}}{\partial x_i} = -\frac{\partial (\overline{p} + 2\rho k_r/3)}{\partial x_j} + \mu \frac{\partial^2 \overline{U}_j}{\partial x_i \partial x_i} - \frac{\partial \tau_{ij}^r}{\partial x_i}, \qquad (23)$$

and a model for the anisotropic residual stress tensor is needed to close the system of equations.

The Smagorinsky subgrid scale model

The *Smagorinsky SGS model* assume that the anisotropic residual stress tensor can be computed as:

$$\tau_{ij}^{r} = -2\nu_{sgs}\overline{S}_{ij},$$

where $\overline{S}$ is the *filtered rate of strain tensor*

$$\overline{S}_{ij} = \frac{1}{2}\left(\frac{\partial \overline{U}_i}{\partial x_j} + \frac{\partial \overline{U}_j}{\partial x_i}\right)$$

and ν_{sgs} is the *subgrid scale viscosity*. The subgrid scale viscosity is calculated as:

$$\nu_{sgs} = C_k \Delta \sqrt{k_{sgs}},$$

where C_k is a model constant with a default value $C_k = 0.094$. The subgrid scale kinetic energy is obtained through a energy equilibrium equation at the subgrid scale that leads to a quadratic equation for k_{sgs}:

$$ak^2 + bk + c = 0,$$

where

- $a = C_e/\Delta$, where C_e is a model constant with default value $C_e = 1.048$,
- $b = 2\overline{S}_{ii}/3$,
- $c = 2C_k\Delta\left(dev\left(\overline{S}\right) : \overline{S}\right)$, with $dev(\overline{S})$ equal to the deviatoric part of $\overline{S}$.

We can notice that we have not applied explicitly a filtering operation and because of that we refer to this model as a *LES with implicit filtering*.

2 THE BIFIDELITY STRATEGY

In many problems represented by a mathematical model, the knowledge of the solution at different values of specific parameters is necessary. One way to proceed is to comupute a high fidelity simulation at each of these points but, if the high fidelity simulation is computational demanding, this if often too time consuming. A bifidelity strategy is useful when it is available a low fidelity model, less accurate than the high fidelity one, but still able to resolve the meain feature of the problem producing qualitative prediction with cheaper computation cost. A bifidelity strategy could be useful, for example, to deal with optimization problems,uncertainty quantification techniques or even preliminary design tests.

In our case, the specific aim is to reconstruct a surrogate high fidelity solution of the problem (5), for a specific Reynolds number, without execute the relative simulation. The high fidelity simulation is time demanding and this is why we are trying to use a different approach. The main conceptual steps of the procedure are the following:

1. make several low fidelity simulations, which is relatively a fast task, for a wide range of Reynolds numers and store them;

2. using these simulations, we use a selection procedure to find the Reynolds numbers where we have to compute the high fidelity simulations. Of course, they must be a small number with respect to the low fidelity simulations;

3. define an interpolant operator which allows us to obtain a surrogate high fidelity simulation featuring a new Reynolds number just using the corresponding low fidelity simulation and the high fidelity simulations previously stored.

2.1 THE GENERAL PROBLEM

First, we introduce a general description of the bi-fidelity strategy based on the work of [Zhu-Narayan-Xiu], [Narayan-Gittelson-Xiu] and [Canuto-Pieraccini-Xiu]. As we anticipated, the strategy poses is well suited to a differential system dependendent on one or more parameters. Let us consider a function u defined on the set $D \subseteq \mathbb{R}^d$ and depending on a parameter $z \in I_Z$ and consider the following problem:

$$\begin{cases} u_t(\boldsymbol{x}, t, Z) = \mathcal{L}(u) & D \times (0, T] \times I_Z, \\ \mathcal{B}(u) = 0 & \partial D \times [0, T] \times I_Z, \\ u = u_0 & D \times \{t = 0\} \times I_Z, \end{cases}$$

where

- $\mathcal{L}$ is a differential operator,
- $\mathcal{B}$ is a boundary condition operator,
- u_0 is the initial condition,
- $D \subset \mathbb{R}^l$ is a physical domain with coordinates $\boldsymbol{x} = (x_1, ..., x_l)$,
- $t \in [0, T]$ is the temporal domain, with $T > 0$,
- $Z = (Z_1, Z_2, ..., Z_d) \in I_Z \subseteq \mathbb{R}^d$ is a parameter domain.

Fixed a particular value of the parameters $z \in I_Z$, we can compute a numerical solution for the problem, whose distance from the solution $u(\boldsymbol{x}, t, z)$ depends on the accuracy of the numerical simulation. Of course, if the parameters change their values, we need to recompute the numerical solution because the solution is different.

2.1.1 High fidelity and low fidelity simulation

The difference between a high fidelity simulation and a low fidelity simulation is simple: the first one is more accurate, but computationally expensive, while the latter is less accurate, but less expensive to compute. This gap can be due to a different model used during the simulation, different meshes, linearizations or different approximation techniques.

We denote $u^H(z)$, with $z \in I_Z$, a high fidelity approximation of the exact solution $u(z)$, in particular:

$$u^H : I_Z \to V^H$$

where V^H is a Hilbert space with inner product $\langle \cdot, \cdot \rangle^H$ and it is the approximation space for the high fidelity solution. We remember that a Hilbert space is an inner product space which is also a complete metric space with respect to the distance function defined by the inner product. It stands that each finite dimensional vector space equipped with inner product is also a Hilbert space. Similarly, we denote $u^L(z)$, with $z \in I_Z$, a low-fidelity approximation of the exact solution $u(z)$, in particular:

$$u^L : I_Z \to V^L$$

where V^L is a Hilbert space with inner product $\langle \cdot, \cdot \rangle^L$ and it is the approximation space for the low-fidelity solution. It stands that $dim(V^L) << dim(V^H)$.

In our case, the high fidelity simulations and the low fidelity simulations are computed through a *CFD* software based on finite volume method. This means that the domain of the problem is subdivided into cells and, in each cell centroid, the value for pressure and velocity will be computed. So, the generic simulation result will be a list of values in the cell centroids interpretable as a vector. For convenience, we will represent them in bold: $\boldsymbol{u^H}$, $\boldsymbol{u^L}$.

2.2 FIND THE HIGH FIDELITY SIMULATIONS NEEDED

We will use the following notations:

- $\Gamma = \{z_1, ..., z_M\} \subset I_Z$ is a set of sample points in I_Z with cardinality M, at which we will compute the low fidelity simulations. It is assumed to contain a large number of sample points such that the set I_Z is well represented;
- $\gamma_N = \{z_1, ..., z_N\} \subset \Gamma$ is a set of sample points in I_Z with cardinality N, where $N << M$, at which we will compute the high fidelity simulations;

- $u^L(\Gamma) = \{\boldsymbol{u^L}(z_1), ..., \boldsymbol{u^L}(z_M)\}$ is a set containing all the low fidelity simulations;
- $U^L(\Gamma) = span(u^L(\Gamma)) = span\{\boldsymbol{u^L}(z_1), ..., \boldsymbol{u^L}(z_M)\}$ is the vector space generated by the low fidelity simulations;
- $u^H(\gamma_N) = \{\boldsymbol{u^H}(z_1), ..., \boldsymbol{u^H}(z_N)\}$ is a set containing all the high fidelity simulations corresponding to parameters in γ_N;
- $U^H(\gamma_N) = span(u^H(\gamma_N)) = span\{\boldsymbol{u^H}(z_1), ..., \boldsymbol{u^H}(z_N)\}$ is the vector space generated by the high fidelity simulations;
- $\boldsymbol{Z} \in \mathbb{R}^{M \times d}$ is the matrix whose rows are the set of sample points $z_i \in \Gamma$.

The first step is to compute a large number of low fidelity simulations and store them. Now we discuss the alghoritm used to find the optimal set of values γ_N to perform the high-fidelity simulations. To find γ_N a greedy algorithm is used: starting from $\gamma_0 = \{\}$ we add one sample point z_k, for each step $k = 1, ..., N$ of the iteration, at the set of sample points γ_{k-1}; z_k is the sample point that maximise the distance between the corresponding solution $\boldsymbol{u^L}(z_k)$ and the vector space $U^L(\gamma_{k-1}) = span(u^L(\gamma_{k-1})) = span\{\boldsymbol{u^L}(z_1), ..., \boldsymbol{u^L}(z_{k-1})\}$:

$$\gamma_k = \gamma_{k-1} \cup \{z_k\} \tag{24}$$

$$z_k = \underset{z \in \Gamma}{argmax} \left(dist(\boldsymbol{u^L}(z), U^L(\gamma_{k-1})) \right) \tag{25}$$

In order to do that, we exploit some linear algebra. There are different ways to proceed but the most efficient, as it is illustrated in [Narayan-Gittelson-Xiu], is to go through a pivoted Cholesky decomposition:

- let $\boldsymbol{W} \in \mathbb{R}^{M,M}$ be the scalar product matrix of the low fidelity simulations, such that $w_{ij} = \langle \boldsymbol{u^L}(z_i), \boldsymbol{u^L}(z_j) \rangle^L$;
- we can express $\boldsymbol{W}$ using a generic basis set $\{\boldsymbol{b_k}\}_{k=1}^{N_L}$ of the V_L space:

$$\boldsymbol{u^L}(z_i) = \sum_{k=1}^{N_L} \hat{v}_k^L(z_i) \boldsymbol{b_k}(x) = \boldsymbol{B}\hat{\boldsymbol{v}}(z_i)$$

where

$$\hat{\boldsymbol{v}}(z_i) = [\hat{v}_1^L(z_i), ..., \hat{v}_{N_L}^L(z_i)]^T \in \mathbb{R}^{N_L \times 1}$$
$$\boldsymbol{B} = [\boldsymbol{b_1}(x), ..., \boldsymbol{b_{N_L}}(x)] \in \mathbb{R}^{N_L \times N_L}$$

introducing the Gramian matrix $\boldsymbol{G} \in \mathbb{R}^{N_L \times N_L}$

$$\boldsymbol{G} = (g_{lk})_{1 \leq l,k \leq N_L} \qquad g_{lk} = \langle \boldsymbol{b_l}(x), \boldsymbol{b_k}(\boldsymbol{x}) \rangle^L$$

and

$$\boldsymbol{V} = [\hat{\boldsymbol{v}}(z_1), ..., \hat{\boldsymbol{v}}(z_M)] \in \mathbb{R}^{N_L \times M}$$

we obtain that

$$\boldsymbol{W} = \boldsymbol{V}^T \boldsymbol{G} \boldsymbol{V} \tag{26}$$

- we point out that, using results originated from a finite volume method, it is natural to use a canonical base such that $\boldsymbol{G} = \boldsymbol{I}$ and the columns of $\boldsymbol{V}$ are our low fidelity simulation data for a fixed sample point in I_Z;
- once $\boldsymbol{W}$ is known, we execute a pivoted Cholesky decomposition of $\boldsymbol{W} = \boldsymbol{V}^T \boldsymbol{G} \boldsymbol{V}$ such that $\boldsymbol{W} = \boldsymbol{P}^T \boldsymbol{L} \boldsymbol{L}^T \boldsymbol{P}$. It is not necessary to complete the decomposition in its entirety, but it is sufficient to execute the first N steps of the decomposition alghoritm;
- once the *permutation matrix* $\boldsymbol{P} \in \mathbb{R}^{M \times M}$ is found, we can compute $\boldsymbol{PZ}$. The first N rows of $\boldsymbol{PZ}$ are the set of sample points γ_N. Again, only information from the first rows/-columns of P are enough.

The alghoritm that perform the pivoted Cholesky decomposition, provided by [Zhu-Narayan-Xiu], is implemeted in Matlab and reported in listing 2.1. Obtained the set γ_N, we can compute the correspondents N high fidelity simulations and store them. Proceeding in this way $u_L(\gamma)$ forms a linearly independent set of solutions.

Listing 2.1: Sample of selection alghoritm Matlab code

```
% Input: V, M, N, B (=I if not specified)
% Output: L, Pe (permutation vectors), V_new (permuted
    V)
```

```
for k=1:M
      w(k)=V(:,k)'*B*V(:,k);
end
% Initializations
Pe=1:M;
L=zeros(M,N);
for n=1:N
    % e is the max, p is the max index
    [e,p]=max(w(n:M));
    p=p+n-1;
    % Exchange n and p coloumns in V
    V(:,[n p])=V(:,[p n]);
    % Exchange n and p elements in w
    w([n p])=w([p n]);
    % Exchange n and p rows in L$
    L([n p],:)=L([p n],:);
    % Exchange n and p elements in Pe
    Pe([n p])=Pe([p n]);
    % Update L and w
    for t=n+1:M
        r(t)=V(:,t)'*B*V(:,n)-L(t,1:N-1)*L(n,1:N-1)';
    end
    L(n,n)=sqrt(w(n));
    L(n+1:M,n)=r(n+1:M)/L(n,n);
    w(n+1:M)=w(n+1:M)-L(n+1:M,n)'.^2;
end
% Truncate the Cholesky factor
L=L(1:n,:);
% Compute the truncated Gramian matrix GL
GL=L*L';
% Update V (the firsts N columns are the low fidelity
    simulations correspondents to the N set of sample
    points selected)
V_new=V;
```

2.3 DEFINING THE INTERPOLANT OPERATOR

At this point we have:

- M low fidelity simulations computed using the set of parameter samples contained in $\Gamma = \{z_1, ..., z_M\} \subset I_Z$,
- N high fidelity simulations computed using the set of parameter samples contained in $\gamma_N = \{z_1, ..., z_N\} \subset \Gamma$ obtained through the pivoted Cholesky decomposition.

The goal is to define an interpolant operator that, from a new generic low fidelity simulation $\boldsymbol{u^L}(z)$, allows us to reconstruct a surrogate high fidelity simulation $\boldsymbol{v^H}(z)$. It will be worth using a bifidelity strategy in this type of problem if $\boldsymbol{v^H}(z)$ is a good approximation of the true corresponding high fidelity simulation $\boldsymbol{u^H}(z)$.

The idea used in the construction of the interpolant operator is the following:

- find the best approximation of the generic $\boldsymbol{u^L}(z)$ in the space $U^L(\gamma_N)$,
- use the same interpolation rule in the space $U^H(\gamma_N)$.

Let us consider the Hilbert space $U^L(\gamma_N)$ and the Hilbert space V^L; we can define the *orthogonal complement* of $U^L(\gamma_N)$ as the set of vectors of V^L orthogonal at each element of $U^L(\gamma_N)$:

$$\left(U^L(\gamma_N)\right)^{\perp} := \left\{\boldsymbol{\eta} \in V^L | \, \langle \boldsymbol{\eta}, \boldsymbol{\phi} \rangle^L = 0, \forall \boldsymbol{\phi} \in U^L(\gamma_N)\right\}.$$

It can be demonstrated that, for each $\boldsymbol{\varphi} \in V^L$, exists exactly one $\boldsymbol{\phi} \in U^L(\gamma_N)$ such that:

$$\boldsymbol{\varphi} = \boldsymbol{\phi} + \boldsymbol{\eta}, \quad \textit{with } \boldsymbol{\eta} \in (U^L(\gamma_N))^{\perp},$$

where $\boldsymbol{\phi}$ is the *orthogonal projection* of $\boldsymbol{\varphi}$ on $U^L(\gamma_N)$ and $\boldsymbol{\eta}$ is the *residual vector*. It stands that

$$||\boldsymbol{\varphi} - \boldsymbol{\phi}|| \leq ||\boldsymbol{\varphi} - \boldsymbol{\phi}'|| \quad \forall \boldsymbol{\phi}' \in U^L(\gamma_N),$$

so $\boldsymbol{\phi}$ is the element of V^L with minimum distance from $\boldsymbol{\varphi}$.

Then, let z be a generic sample point in I_z which doesn't necessarily belong to Γ; the best approximation of $\boldsymbol{u^L}(z)$ in $U^L(\gamma_N)$ is the projection of $\boldsymbol{u^L}(z)$ on $U^L(\gamma_N)$. The generic element of $U^L(\gamma_N)$ can be expressed using the independent linear set $\boldsymbol{u^L}(z_k)$ as basis

$$\boldsymbol{\phi} = \sum_{j=1}^{N} c_j \boldsymbol{u^L}(z_j)$$

and, in order to find the projection of $\boldsymbol{u^L}(z)$, it is sufficient that the residual vector is orthogonal to each basis vector $\boldsymbol{u^L}(z_k)$:

$$\left\langle \boldsymbol{u^L}(z) - \sum_{j=1}^{N} c_j \boldsymbol{u^L}(z_j), \boldsymbol{u^L}(z_i) \right\rangle^L = 0$$

$$\sum_{j=1}^{N} c_j \left\langle \boldsymbol{u^L}(z_j), \boldsymbol{u^L}(z_i) \right\rangle^L = \left\langle \boldsymbol{u^L}(z), \boldsymbol{u^L}(z_i) \right\rangle^L, \quad \forall i = 1, ..., N.$$

which, in matricial form, is:

$$\boldsymbol{G^L c} = \boldsymbol{g} \tag{27}$$

where $\boldsymbol{G^L}$ is the truncated Gramian matrix and

$$\boldsymbol{g} = (g_i)_{1 \le i \le N}, \qquad g_i = \left\langle \boldsymbol{u^L}(z), \boldsymbol{u^L}(z_i) \right\rangle^L$$

Eventually, we define

$$\boldsymbol{v^H}(z) = \sum_{k=1}^{N} c_k \boldsymbol{u^H}(z_k). \tag{28}$$

This complete the procedure, which is summarized in listing 2.2.

Listing 2.2: Sample of reconstruction alghoritm Matlab code

```
% Input: L, V_new, VHF (matrix of available HF
    simulations), N, vz (vector to be reconstructed), B
    (=I if not specified)
% Output: vzHF (surrogate HF reconstructed), cc (
    interpolation coefficients)
Vtilde=V(:,1:N);
g=Vtilde'*B*vz;
% Solve (L')*L*cc=g
cc=(L')\(L\g);
vzHF=VHF*cc;
```

3 LID DRIVEN CAVITY FLOW

In the second part of this thesis we will apply the *bifidelity strategy* to two common fluid dynamics testcases, which are:

- *lid driven cavity flow*,
- *backward facing step*.

All the simulations are performed with *OpenFoam*, an opensource computational fluid dynamics software based on finite volume method. The simulations are runned on a laptop equipped with a *Intel® Core™ i7-7700HQ processor*, featuring four cores and a processor base frequency of $2.80\,GHz$. Anyway, since the lid driven cavity flow is a simple testcase, we haven't implemented parallel computation and just one core has been used.

3.1 DESCRIPTION OF THE FLOW

The lid driven cavity flow is a simple testcase that consists in a sqare box whose top wall moves with a constant velocity. The case is bidimensional and the domain is a square with a $1\,m$ side represented in a cartesian coordinate system with the bottom left corner as origin. Walls are denoted as *bottom wall*, *right wall*, *top wall* and *left wall*.

We are interested in the stationary solution of an incompressible laminar flow and, because of that, the Reynolds number simulated are low and included in the range $(100 \div 1000)$. The velocity of the lid is easily calculated:

$$Re = \frac{U_{lid} L}{\nu} \;\rightarrow\; U_{lid} = \frac{Re\,\nu}{L},$$

where $L = 1\,m$ is the charateristic length of the problem and $\nu = \mu/\rho = 0.001\,m^2/s$ is the cinematic viscosity.

The corresponding solver in Openfoam that allows us to perform this type of simulation is the *SimpleFoam* solver with a

laminar simulation type option, which solves the incompressible Navier Stokes system of equation using the *SIMPLE* (Semi Implicit Method for Pressure Linked Equations) alghorithm without an additional treatment of turbulent phenomena. The results of a simulation are a list of values of the velocity vector (U_x, U_y) and a list of values of p, which correspond to the values in the cell centroids of the mesh. However, the values of p are not the pressure but the pressure divided by density, called *kinematic pressure*, and its unit of measure is $[m^2/s^2]$. Due to this, from now on, we will let p denote the pressure divided by density.

The solution of this testcase is well documentend (see, for example, [Ghia-Ghia-Shin]): we expect a large vortex in the center of the box and smaller ones at the edges and the whole flowfield is strongly Reynolds number dependent. This is evident in figure 1, where the *streamlines* are represented. Streamlines are the lines tangent to the velocity vector and they correspond to the path of the fluid particles. They are caluculated from the velocity field with a *Runge Kutta* method in Paraview.

Intial conditions in the domain are:

- $\boldsymbol{U} = 0\, m/s$,
- $p = 0\, m^2/s^2$.

Boundary conditions are:

- *no-slip condition* at left wall, bottom wall and right wall, such that the velocity at the boundary is $\boldsymbol{U_b} = 0\, m/s$ (a no-slip condition imposes that the relative velocity at the boundary is zero),
- *fixed value* velocity $\boldsymbol{U}_{lid} = (U_{lid}, 0, 0)$ at the top wall,
- *zero gradient* condition for p at all the walls.

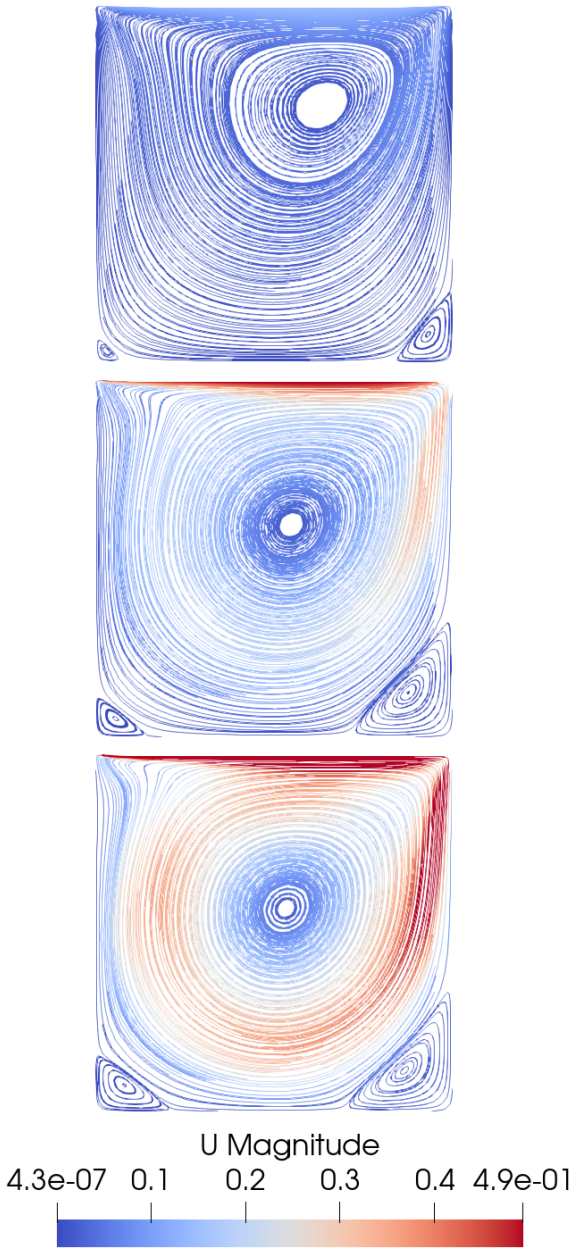

Figure 1: Visualization of streamlines at different Reynolds numbers. Top to bottom: $Re = 150, 550, 950$.

3.2 A MENTION OF SIMPLE ALGORITHM IMPLEMENTATION

The *SimpleFoam* solver solves the incompressible Navier Stokes system (3):

$$\begin{cases} \nabla \cdot \boldsymbol{U} = 0 \\ \rho \dfrac{\partial \boldsymbol{U}}{\partial t} + \rho \nabla \cdot (\boldsymbol{U}\boldsymbol{U}) = -\nabla p + \nabla \cdot (\mu \nabla \boldsymbol{U}). \end{cases}$$

An application of a finite volume method to the momentum equations yields an algebraic system, which can be written in a *semi-discretized* form:

$$\boldsymbol{A}\boldsymbol{U} = \boldsymbol{H}(\boldsymbol{U}) - \nabla p,$$

where

- $\boldsymbol{A}$ is a diagonal matrix,
- $\boldsymbol{H}(\boldsymbol{U})$ contains the off-diagonal contributions.

This equation can be solved iteratively using an initial guess for the pressure or the values resulting from a previous iteration:

$$\boldsymbol{U} = \boldsymbol{A}^{-1}\boldsymbol{H}(\boldsymbol{U}) - \boldsymbol{A}^{-1}\nabla p. \tag{29}$$

The continuity equation is used to get an equation for the pressure:

$$\nabla \cdot \boldsymbol{U} = 0 \quad \Rightarrow \quad \nabla \cdot (\boldsymbol{A}^{-1}\boldsymbol{H}(\boldsymbol{U}) - \boldsymbol{A}^{-1}\nabla p) = 0,$$

and

$$\nabla \cdot (\boldsymbol{A}^{-1}\nabla p) = \nabla \cdot (\boldsymbol{A}^{-1}\boldsymbol{H}(\boldsymbol{U})). \tag{30}$$

Solving this equation for p leads to a new pressure field that satisfy $\nabla \cdot \boldsymbol{U} = 0$, but now the momentum equation is no longer verified and a certain number of iterations in this *outer loop* are needed to reach the convergence. Then we can define the residual of an algebraic system; considering the generic system of equations $\boldsymbol{A}\boldsymbol{x} = \boldsymbol{b}$, we can define the cell residuals as

$$\boldsymbol{r} = \boldsymbol{b} - \boldsymbol{A}\boldsymbol{x}.$$

The *scaled residual* is computed from the mean value of the solution vector $\overline{\boldsymbol{x}}$ and $n = \sum_i \left(|\boldsymbol{A}\boldsymbol{x} - \boldsymbol{A}\overline{\boldsymbol{x}}|_i + |\boldsymbol{b} - \boldsymbol{A}\overline{\boldsymbol{x}}|_i \right)$ as:

$$r = \frac{1}{n} \sum |\boldsymbol{b} - \boldsymbol{A}\boldsymbol{x}|.$$

A similar concept is used to define the residuals for pressure and velocity using the matrix equations (29) and (30).

3.3 LOW FIDELITY AND HIGH FIDELITY SIMULATIONS

As anticipated, we need to perform several (fast) low fidelity simulations and a low number of accurate high fidelity simulations. Since we have used the same mathematical model for both, the only difference will be in the computational grid:

- the low fidelity mesh is a 30×30 grid, with 900 total cells and a cell side of $1/30\,m$;
- the high fidelity mesh is a 250×250 grid, with 62500 total cells and a cell side of $1/250\,m$.

Using a residual control on the scaled residuals of 10^{-4} on p and $\boldsymbol{U}$ a low fidelity simulation will converge in approximately 3 seconds, while a high fidelity simulation will converge in 120 seconds, which is two orders of magnitude greater. The low fidelity mesh and the high fidelity mesh are represented in Figures 2 and 3.

3.4 RECONSTRUCTION

We have performed 46 low fidelity simulations with Reynolds number in the range $(100 \div 1000)$, each Re spaced apart from the previous one by a $\Delta Re = 20$. We have reconstructed three high fidelity surrogate simulations:

- $Re = 150$,
- $Re = 550$,

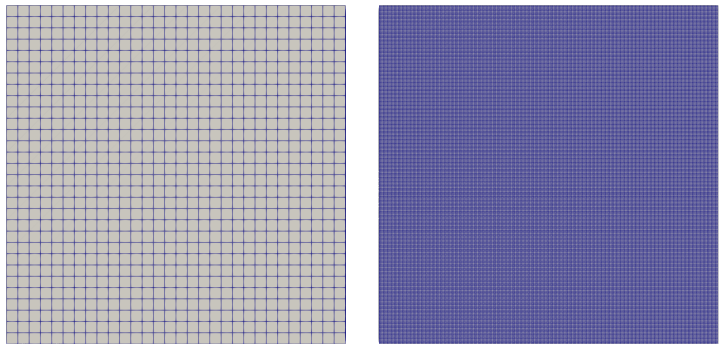

Figure 2: Difference between the low fidelity mesh (left) and the high fidelity mesh (right).

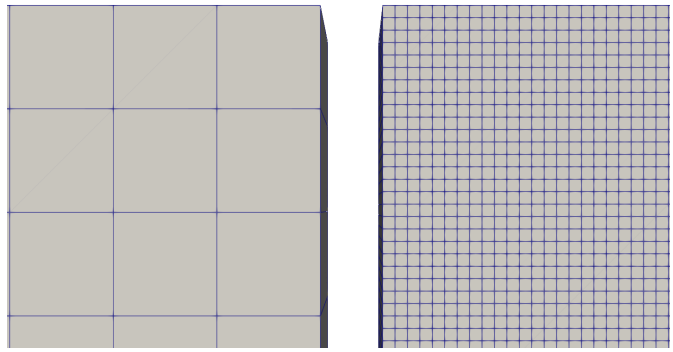

Figure 3: Detail about the difference between the two meshes.

- $Re = 950$.

These Reynolds numbers did not belong to the initial low fidelity simulations database. For each of them we used a number of high fidelity simulations in the reconstruction process between 1 and 10. The reconstruction of the kinematic pressure and the reconstruction of the velocity are performed independently.

3.4.1 Reconstruction of the kinetic pressure field

Using the bifidelity strategy described in chapter 2, we will seek for:

- the Reynolds numbers at which we need to compute the high fidelity simulations (script 2.1),
- the reconstruction coefficients (script 2.2).

For example, considering $Re = 150$ and $N = 3$ high fidelity simulations, as we can see from Table 2, the surrogate high fidelity simulation is calculated as illustrated in equation (28):

$$\boldsymbol{v}^{\boldsymbol{H}}_{150} = 0.020\boldsymbol{u}^{\boldsymbol{H}}_{1000} - 0.126\boldsymbol{u}^{\boldsymbol{H}}_{560} + 0.868\boldsymbol{u}^{\boldsymbol{H}}_{220}.$$

In all the tables coefficents are rounded off to the third decimal digit. We can notice that the choice of the Reynolds numbers at which we need to compute the high fidelity simulations is indipendent on the simulation that we want to reconstruct, so they are the same in all the three cases ($Re = 150$, $Re = 550$, $Re = 950$). In fact, the selection phase is performed priorly and it is based on the ability to span the space V^H.

The results are visualized in *Paraview*, a data analysis open source software. In all the screens, reported in Figures 4, 5 and 6, are represented:

- the true high fidelity simulation at the top left,
- a surrogate high fidelity simulation obtained using five high fidelity simulations at the top center,
- a surrogate high fidelity simulation obtained using three high fidelity simulations at the top right,

$Re = 150$		
N	Re_{HF} used	Coefficients
5	1000	-0.041
	560	-0.145
	220	0.516
	100	0.617
	800	0.122
3	1000	0.020
	560	-0.126
	220	0.868
2	1000	-0.079
	560	0.315
1	1000	0.020

Table 2: Number of high fidelity simulations used, their Reynolds number and the respective coefficients in the reconstruction process of the kinematic pressure in the case of $Re = 150$.

- a surrogate high fidelity simulation obtained using two high fidelity simulations at the bottom left,
- a surrogate high fidelity simulation obtained using one high fidelity simulation at the bottom center,
- the corresponding low fidelity simulation at the bottom right.

In this case the pressure is characterized by a small range of values and the visualization isn't optimal: it is scarely visible a little depression region in the center of the domain, an overpressure region at the top right corner and a depression region at the top left corner.

3.4.2 Reconstruction of the velocity field

The solution of a generic simulation is given through two list of values: one for the horizontal velocity $\boldsymbol{u_x}$ and one for the vertical velocity $\boldsymbol{u_y}$. Considering the generic simulation, the reconstruction process will be performed using as generic low fidelity input a single vector $\boldsymbol{u^L} = [\boldsymbol{u_x^{LF}}; \boldsymbol{u_y^{LF}}]$ and as generic high fidelity input a single vector $\boldsymbol{u^H} = [\boldsymbol{u_x^{HF}}; \boldsymbol{u_y^{HF}}]$.

$Re = 550$		
N	Re_{HF} used	Coefficients
5	1000	0.017
	560	1.033
	220	0.010
	100	0.008
	800	-0.061
3	1000	-0.006
	560	0.980
	220	0.034
2	1000	-0.010
	560	0.997
1	1000	0.302

Table 3: Number of high fidelity simulations used, their Reynolds number and the respective coefficients in the reconstruction process of the kinematic pressure in the case of $Re = 550$.

$Re = 950$		
N	Re_{HF} used	Coefficients
5	1000	0.831
	560	0.311
	220	-0.237
	100	0.076
	800	-0.015
3	1000	0.826
	560	0.287
	220	-0.185
2	1000	0.848
	560	0.194
1	1000	0.908

Table 4: Number of high fidelity simulations used, their Reynolds number and the respective coefficients in the reconstruction process of the kinematic pressure in the case of $Re = 950$.

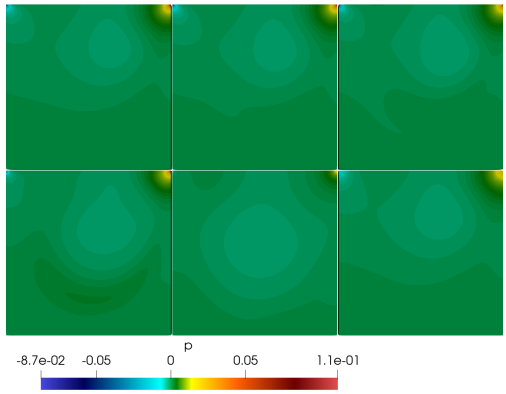

Figure 4: Paraview screen of the kinematic pressure reconstruction at $Re = 150$.

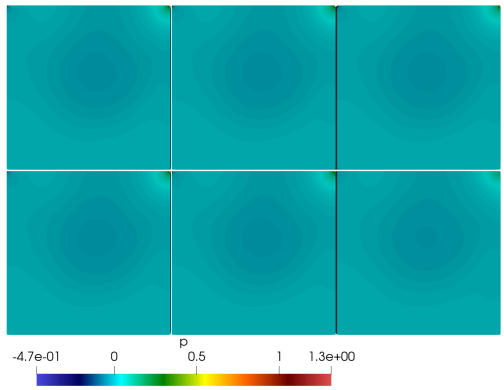

Figure 5: Paraview screen of the kinematic pressure reconstruction at $Re = 550$.

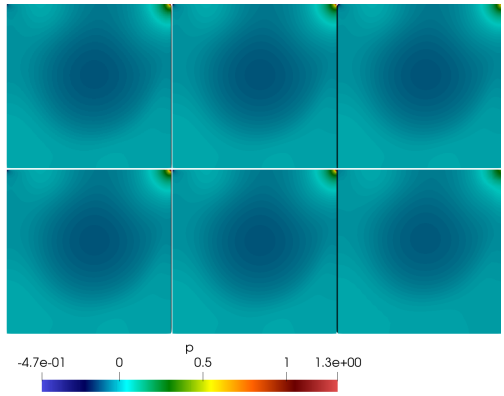

Figure 6: Paraview screen of the kinematic pressure reconstruction at $Re = 950$.

Because of that, taking for example the reconstruction of $Re = 150$ with $N = 3$ high fidelity simulations used, the surrogate high fidelity output is:

$$\boldsymbol{v}^{\boldsymbol{H}}_{150} = -0.004\boldsymbol{u}^{\boldsymbol{H}}_{1000} + 0.044\boldsymbol{u}^{\boldsymbol{H}}_{560} + 0.988\boldsymbol{u}^{\boldsymbol{H}}_{220}.$$

To obtain the reconstructed horizontal velocity $\boldsymbol{v}^{\boldsymbol{H}}_{\boldsymbol{x}}$ and the reconstructed vertical velocity $\boldsymbol{v}^{\boldsymbol{H}}_{\boldsymbol{y}}$ it is necessary to split this vector into two equal parts: the first one will be the horizontal velocity and the latter will be the vertical velocity.

Once that we have the reconstructed velocity field, we can calculate the reconstructed magnitude velocity in each cell centroid i as:

$$\left|\boldsymbol{v}^{\boldsymbol{H}}_{i}(z)\right| = \sqrt{\left(\boldsymbol{v}^{\boldsymbol{H}}_{\boldsymbol{x}}(z)\right)^2_i + \left(\boldsymbol{v}^{\boldsymbol{H}}_{\boldsymbol{y}}(z)\right)^2_i}. \tag{31}$$

Paraview screens of the reconstructions are represented in Figures 7-15.

Some post processing that we can do is visualize the vertical velocity along the horizontal line that splits in two equal parts the domain. The same process can be done with the horizontal velocity along the vertical line that splits in two equal parts the domain. The combination of the two graphs, represented in Figures 16-21, gives us an overview on the big vortex in the center, wich is cleary visible. In Figure 16 ($Re = 150$), at $x \simeq 0.6\,m$, the vertical velocity changes its sign from positive to negative: the vortex spins clockwise as it is expected with a lid moving towards right. The same applies for the horizontal velocity, which is negative from $x = 0\,m$ to $x \simeq 0.7m$ and then it becomes positive. Same considerations can be made at $Re = 550$ and $Re = 950$.

From the velocity field we can also extract the *skin friction*, which is the shear stress tensor component parallel to the wall at $y = 0$. In a bidimensional case, from equation (1):

$$\tau_{wall} = \mu \left(\frac{\partial U_x}{\partial y}\right)_{y=0}. \tag{32}$$

At the wall $\boldsymbol{U} = \boldsymbol{0}\,m/s$ and y is always non-negative, so the sign of τ_{wall} is the same of U_x and this variable can be used to detect ricirculation bubbles. Considering Figures 22 and 23, which represent the τ_{wall} along the bottom wall, we can see a large

$Re = 150$		
N	Re_{HF} used	Coefficients
5	1000	0.006
	360	0.036
	140	1.164
	680	-0.017
	100	-0.198
3	1000	-0.004
	360	0.044
	140	0.988
2	1000	-0.102
	360	0.663
1	1000	0.125

Table 5: Number of high fidelity simulations used, their Reynolds number and the relative coefficients in the reconstruction process of the velocity in the case of $Re = 150$.

region in the center where $\tau_{wall} < 0\, m^2/s^2$: here the horizontal velocity is negative. Also there are two regions, more visible in the case $Re = 950$, where $\tau_{wall} > 0\, m^2/s^2$: they represent the two ricirculation bubbles that spin counterclockwise at the corners visible in Figure 1.

3.5 ERRORS

To evaluate the quality of the reconstruction and how it evolves using a different number of high fidelity simulations, we need to define an error that reflects how much the surrogate high fidelity simulation is similar to the true high fidelity simulation. We use the following notation:

- p_i is the kinematic pressure in the ith cell;
- $(U_x)_i$ is the horizontal velocity in the ith cell;
- $(U_y)_i$ is the vertical velocity in the ith cell;
- $|\boldsymbol{U}|_i$ is the magnitude velocity in the ith cell;
- n is the number of cells in the high fidelity grid.

$Re = 550$		
N	Re_{HF} used	Coefficients
5	1000	-0.113
	360	0.438
	140	-0.317
	680	0.774
	100	0.237
3	1000	0.210
	360	1.119
	140	-0.441
2	1000	0.254
	360	0.843
1	1000	0.543

Table 6: Number of high fidelity simulations used, their Reynolds number and the relative coefficients in the reconstruction process of the velocity in the case of $Re = 550$.

$Re = 950$		
N	Re_{HF} used	Coefficients
5	1000	0.814
	360	-0.033
	140	0.032
	680	0.222
	100	-0.048
3	1000	0.905
	360	0.176
	140	-0.111
2	1000	0.916
	360	0.106
1	1000	0.952

Table 7: Number of high fidelity simulations used, their Reynolds number and the relative coefficients in the reconstruction process of the velocity in the case of $Re = 950$.

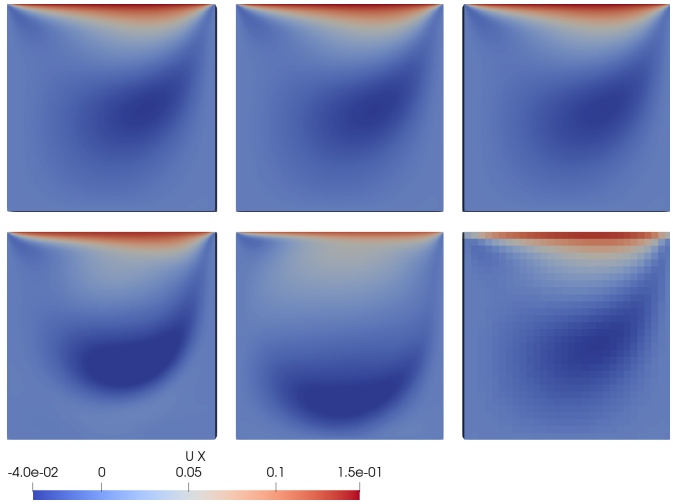

Figure 7: Paraview screen of the horizontal velocity reconstruction at $Re = 150$.

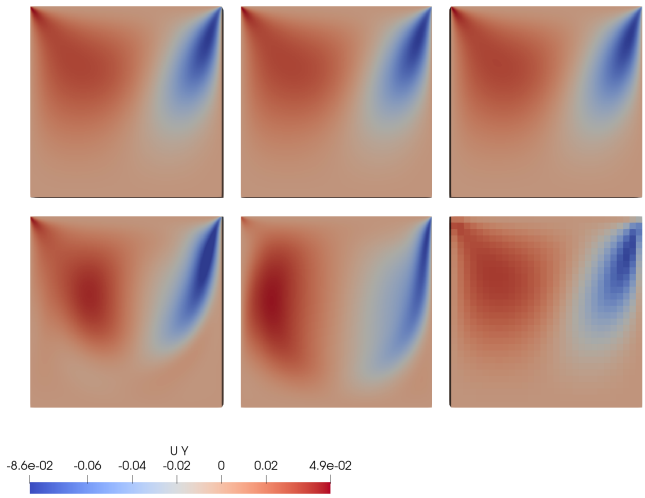

Figure 8: Paraview screen of the vertical velocity reconstruction at $Re = 150$.

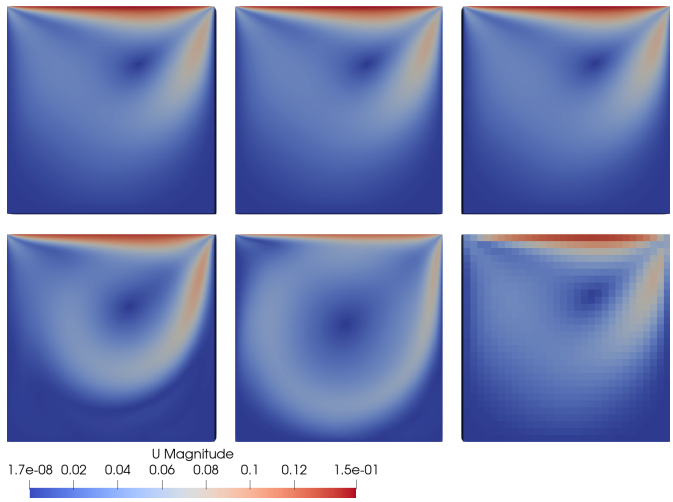

Figure 9: Paraview screen of the velocity magnitude reconstruction at $Re = 150$.

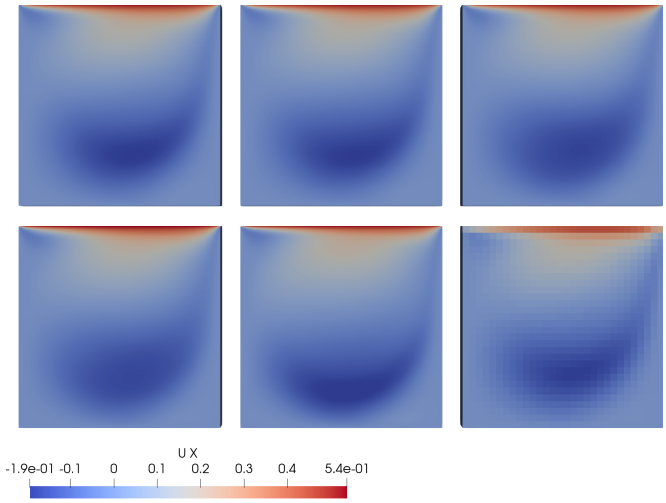

Figure 10: Paraview screen of the horizontal velocity reconstruction at $Re = 550$.

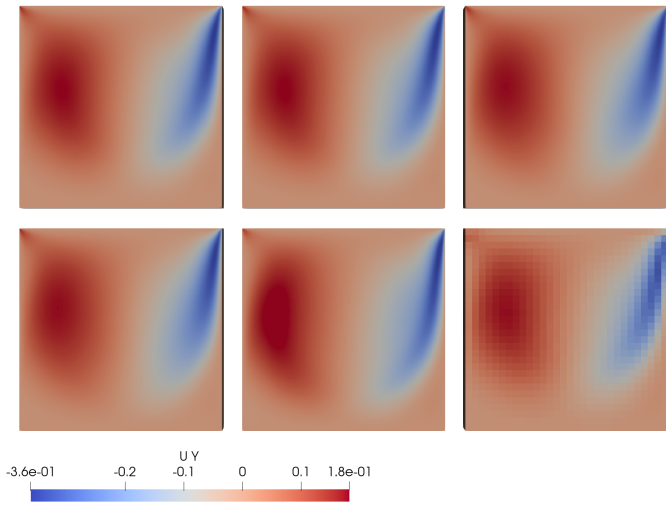

Figure 11: Paraview screen of the vertical velocity reconstruction at $Re = 550$.

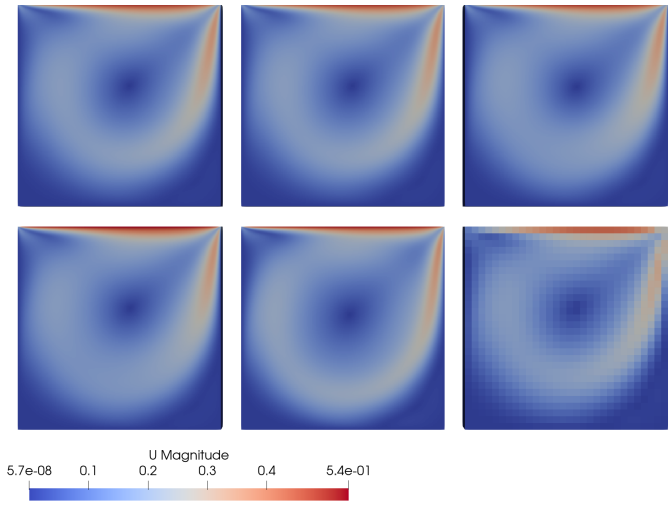

Figure 12: Paraview screen of the velocity magnitude reconstruction at $Re = 550$.

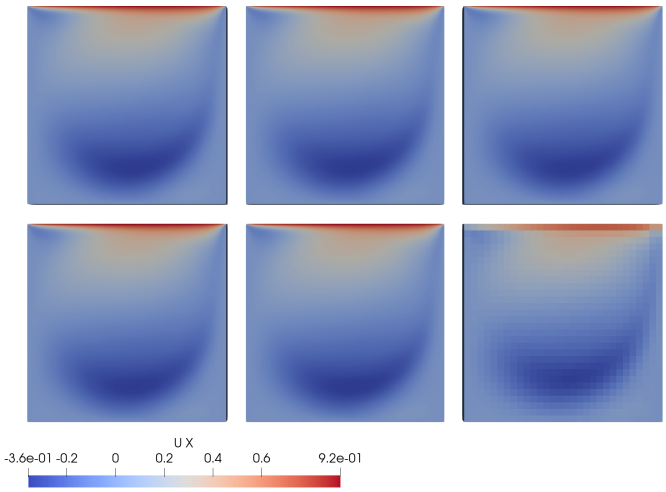

Figure 13: Paraview screen of the horizontal velocity reconstruction at $Re = 950$.

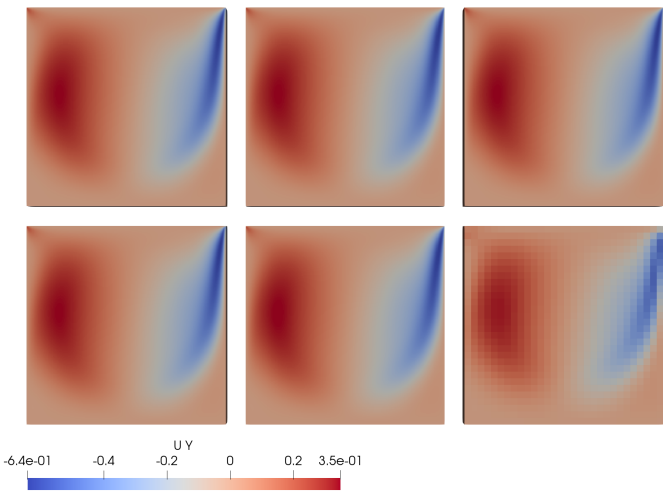

Figure 14: Paraview screen of the vertical velocity reconstruction at $Re = 950$.

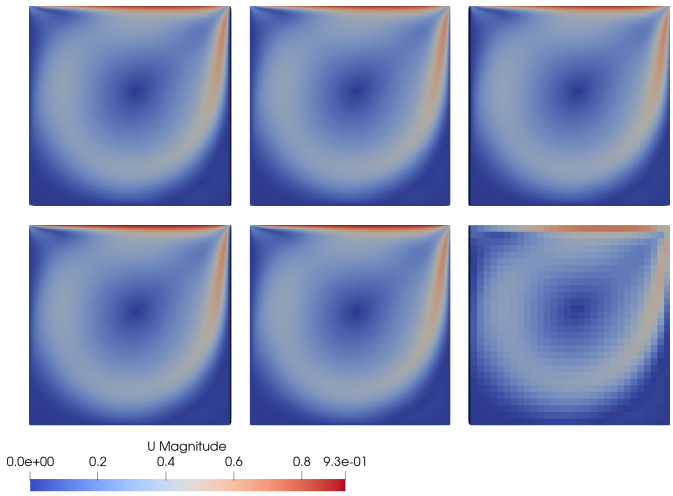

Figure 15: Paraview screen of the velocity magnitude reconstruction at $Re = 950$.

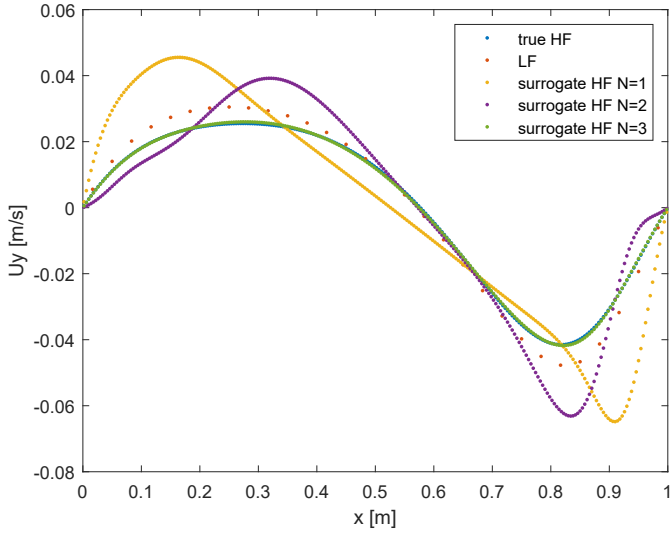

Figure 16: Vertical velocity along an horizontal line that splits the box into two equal parts at $Re = 150$.

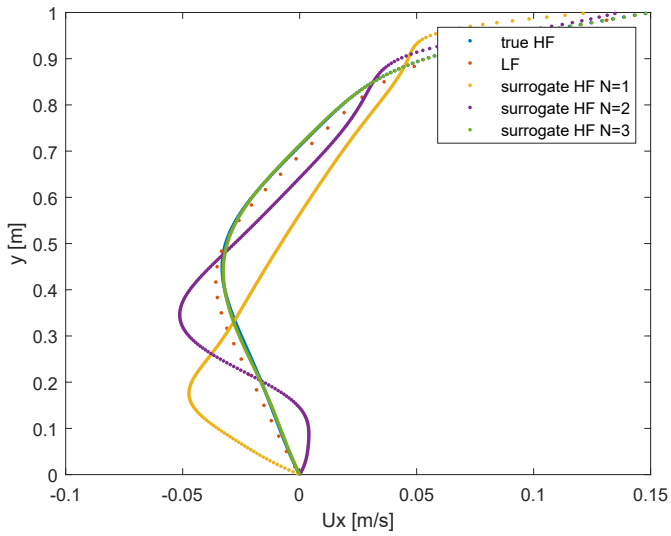

Figure 17: Horizontal velocity along a vertical line that splits the box into two equal parts at $Re = 150$.

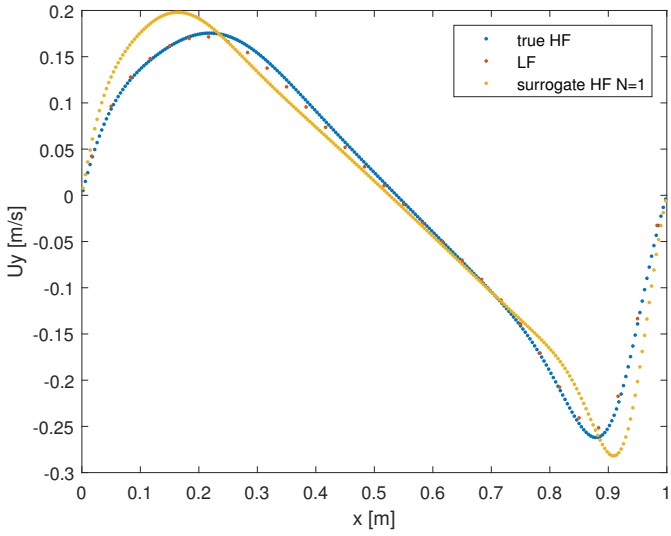

Figure 18: Vertical velocity along an horizontal line that splits the box into two equal parts at $Re = 550$.

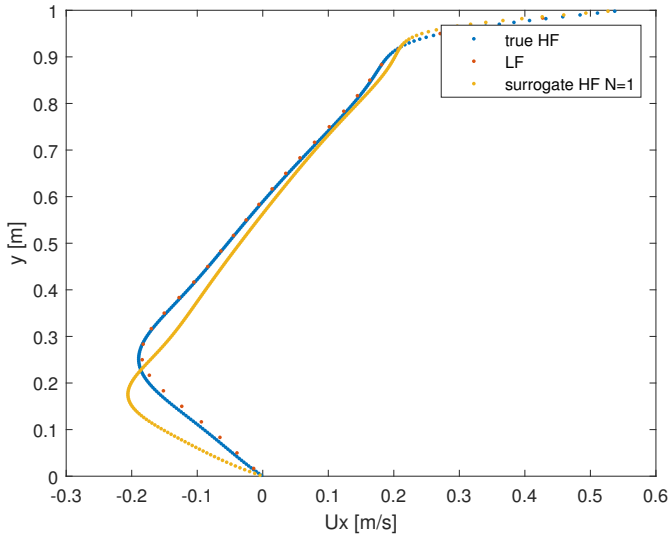

Figure 19: Horizontal velocity along a vertical line that splits the box into two equal parts at $Re = 550$.

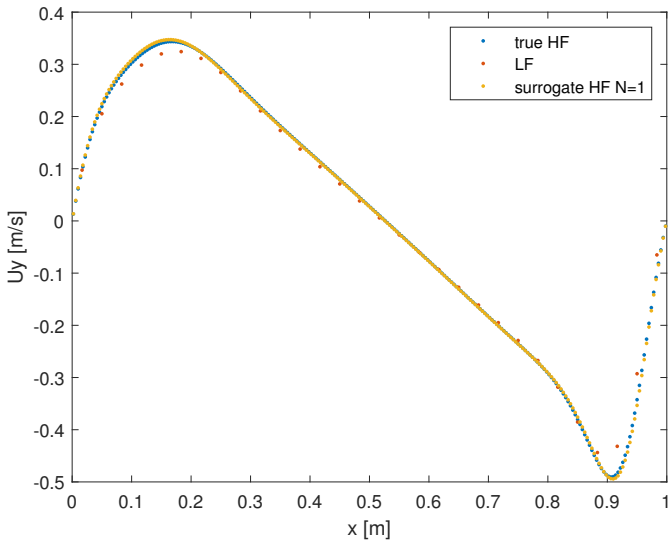

Figure 20: Vertical velocity along an horizontal line that splits the box into two equal parts at $Re = 950$.

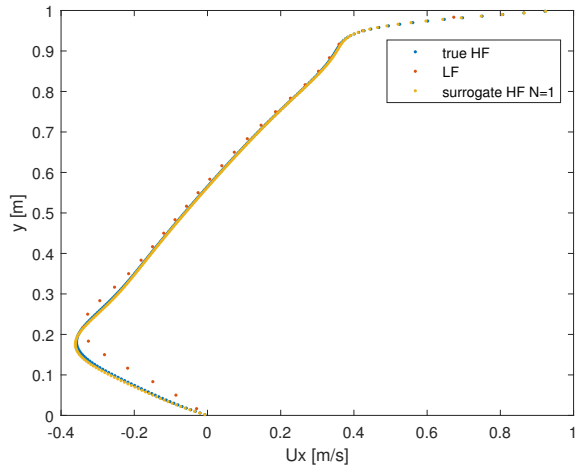

Figure 21: Horizontal velocity along a vertical line that splits the box into two equal parts at $Re = 950$.

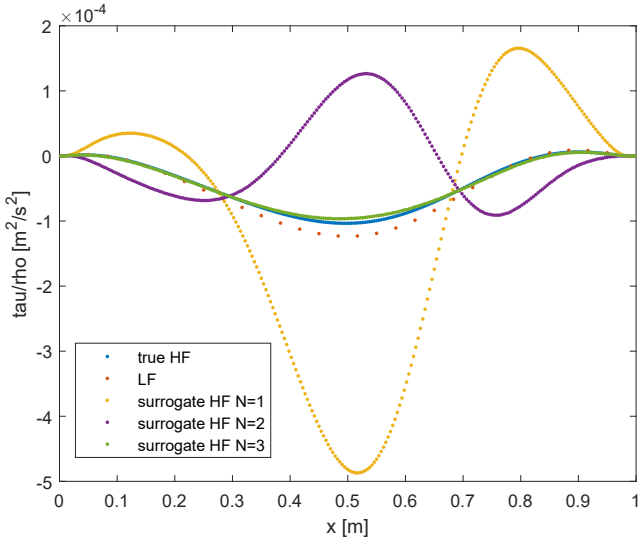

Figure 22: Bottom wall shear stress at $Re = 150$.

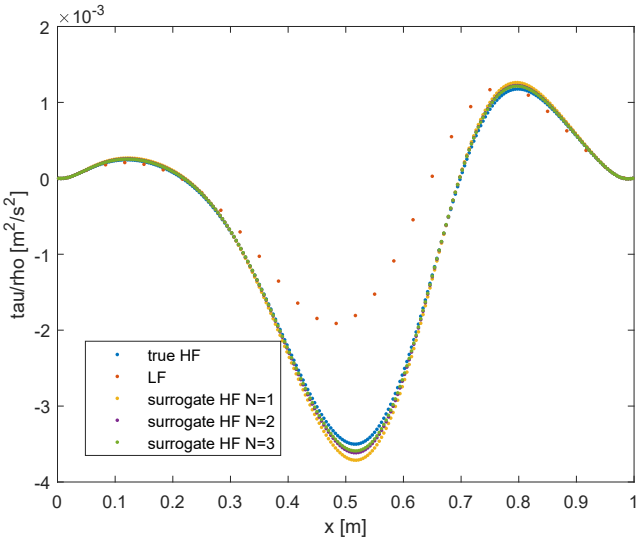

Figure 23: Bottom wall shear stress at $Re = 950$.

We define the kinematic pressure error

$$err_p = \frac{1}{n}\sum_{i=1}^{n}\left(\frac{p_i - p_{i,surrogate}}{U_{lid}^2}\right)^2,$$

the horizontal velocity error

$$err_{U_x} = \frac{1}{n}\sum_{i=1}^{n}\left(\frac{(U_x)_i - (U_x)_{i,surrogate}}{U_{lid}}\right)^2,$$

the vertical velocity error

$$err_{U_y} = \frac{1}{n}\sum_{i=1}^{n}\left(\frac{(U_y)_i - (U_y)_{i,surrogate}}{U_{lid}}\right)^2,$$

and the magnitude velocity error

$$err_{|\boldsymbol{u}|} = \frac{1}{n}\sum_{i=1}^{n}\left(\frac{|\boldsymbol{u}|_i - |\boldsymbol{u}|_{i,surrogate}}{U_{lid}}\right)^2.$$

They are represented in Figures 24-27.

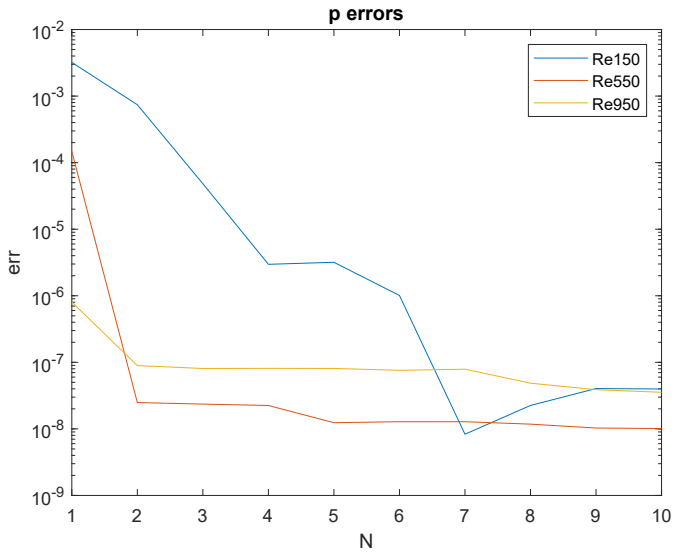

Figure 24: Adimensional error err_p of the surrogate kinematic pressure at different number N of high fidelity simulations used.

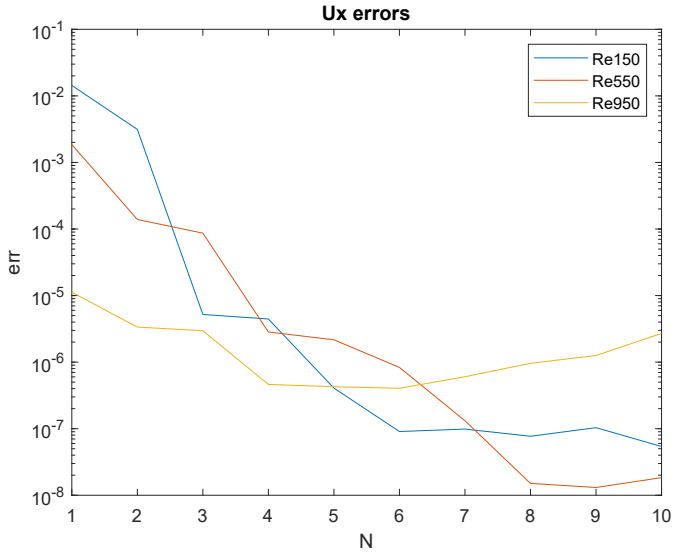

Figure 25: Adimensional error err_{U_x} of the surrogate horizontal velocity at different number N of high fidelity simulations used.

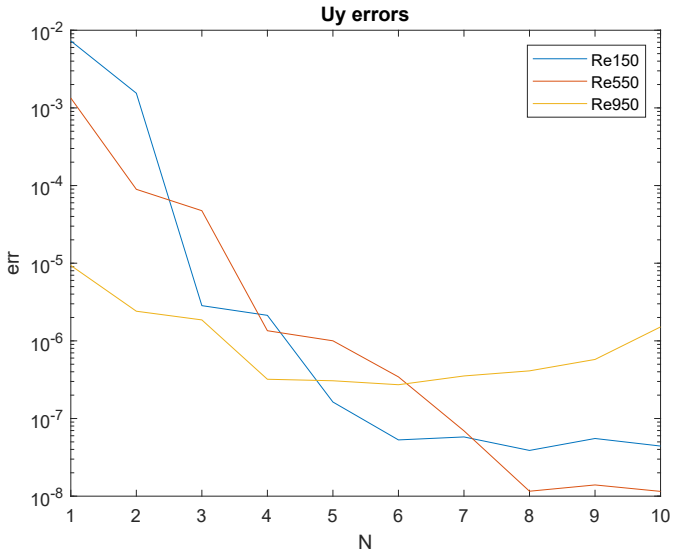

Figure 26: Adimensional error err_{U_y} of the vertical horizontal velocity at different number N of high fidelity simulations used.

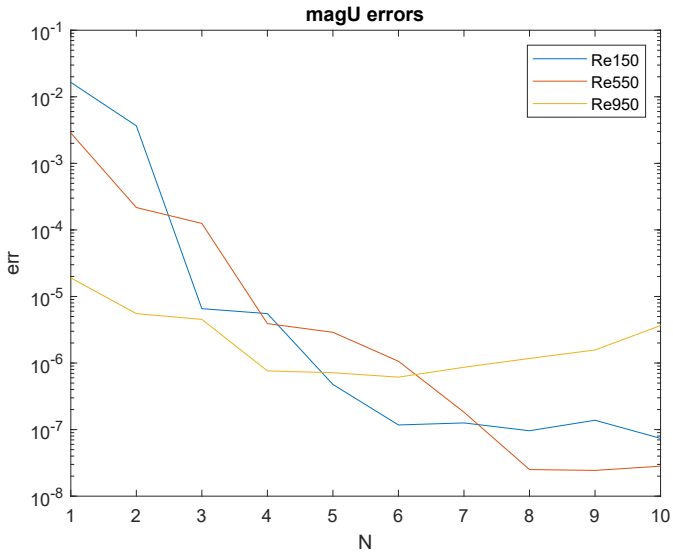

Figure 27: Adimensional error $err_{|\boldsymbol{U}|}$ of the velocity magnitude at different number N of high fidelity simulations used.

3.6 INFLUENCE OF SORTING AND ADIMENSIONALIZATION

In the previous sections we mentioned that the generic result of a simulation is given as a list of values corresponding to the values in the cell centroids of the mesh. The sorting of this values depends on how the mesh is generated: in this case we used a single box and the cell centroids are numerated increasingly from left to right, starting from the lower left corner, and than in the same way keeping on the lines immediately above. The last cell centroid is at the top right.

In order to verify the effect of sorting on the reconstruction process we follow these steps:

- define a permutation vector of the same length of the generic low fidelity simulation and use it to permutate all the low fidelity simulations in input in the same way,
- find the Reynolds number of the high fidelity simulations needed,
- find the interpolation rule using the permutated low fidelity simulations,
- apply the interpolation rule on the high fidelity simulations not permutated.

Proceeding this way we obtain the same Reynolds numbers, the same coefficients and eventually the same errors of the not permutated case, so we are confident that a permutation does not change the results of the reconstruction.

In the previous section we applied the bifidelity stategy using the solution of the dimensional system of incompressible Navier Stokes equations (4). Thinking to hypothetically apply the strategy using the solution of the adimensional system of equations (5), the same boundary condition operator will be applied at all the simulations. In fact, the charateristic velocity is $U_{ref} = U_{lid}$ and the boundary condition at the top wall will be

$$\hat{\boldsymbol{u}}_{\boldsymbol{lid}} = \frac{\boldsymbol{u}_{\boldsymbol{lid}}}{U_{lid}} = (1, 0, 0),$$

while the other boundary conditions remain the same. Anyway, the adimensional velocity, solution of the adimensional system, is nothing but the velocity solution of the dimensional system scaled by the charateristic velocity of the flow, which is U_{lid}. In the same way, the adimensional kinematic pressure, solution of the adimensional system, is the kinematic pressure solution of the dimensional system scaled by a reference value for the kinetic pressure, which is U_{lid}^2. Because of that, we expect that using the bifidelity strategy onto the adimensional system of equation we will get the same Reynolds numbers and the same coefficients of the dimensional case. In order to verify this we follow these steps:

- scale all the low fidelity simulations by the characteristic value of pressure or velocity,
- proceed finding the Reynolds number of the high fidelity simulations needed,
- find the interpolation rule using the adimensional low fidelity simulations,
- apply the interpolation on the scaled high fidelity simulations to get the surrogate adimensional high fidelity simulation,
- multiply the surrogate adimensional high fidelity simulation obtained by the reference value of pressure or velocity,
- compute the errors using the dimensional high fidelity simulations.

Also in this case we obtain the same Reynolds numbers, the same coefficients and eventually the same errors of the dimensional case as expected.

3.7 COMMENTS

From the Paraview screens it is possible to see that the reconstruction of the velocity is qualitatively good using just three

high fidelity simulations. In the case of pressure it is also possible to see that the reconstruction of the kinematic pressure is good using just three high fidelity simulations in the case of $Re = 550$ and in the case of $Re = 950$, while at least five high fidelity simulations are needed in the case $Re = 150$. In fact, errors in the reconstruction of the kinematic pressure are greater in the case at $Re = 150$: considering $N = 3$, we have that $err_{p,Re=150} = 4.82\,10^{-5}$, while $err_{p,Re=550} = 2.36\,10^{-8}$ and $err_{p,Re=950} = 8.08\,10^{-8}$.

The errors general trend, for both velocity and kinematic pressure, consists in an initial sharp decrease followed by a region where the errors show some fluctuations. In certain cases there exists a number of high fidelity simulations used after which the error is almost constant. This is clearly visible, for example, in the reconstruction of the kinematic pressure at $Re = 550$ and $Re = 950$ at $N = 2$ (Figure 24). The only case where the error increases is the reconstruction of the velocity field at $Re = 950$, starting from $N = 6$. It results that using $N = 10$ high fidelity simulations in the reconstruction process leads to the same error of $N = 3$. On the other hand, the case at $Re = 950$ has errors of two orders of magnitude smaller at $N = 1$ and $N = 2$.

Anyway, the errors are low and the reconstruction process works very well. This is also established from the visualizations of the velocity at $Re = 150$ in Figures 16 and 17: in both cases, from $N = 3$, the true high fidelity simulation and the surrogate high fidelity simulation are overlapped. We can notice that the third Re selected, as we can see in Table 5, is $Re = 140$, which is quite close to $Re = 150$ and the respective coefficient is near to one. Something similar happen at $Re = 950$: it is not casual that just one high fidelity simulation is enough to overlap the true high fidelity. In fact, the first Re selected, as we can see in Table 7, is $Re = 1000$, which is quite close to $Re = 950$ and the respective coefficient is near to one. Anyway, also at $Re = 550$ just one high fidelity simulation is sufficient to get the right trend as we can see in Figures 18 and 19.

This means that the low fidelity simulations represent well the behavior of the high fidelity solution in the parameter domain and, because of that, the reconstruction process provides good

results. This is not surprising because the low fidelity simulations get results close to the high fidelity solution.

Also the reconstruction of the wall shear stress, which involves the velocity derivative, is promising. Here we can notice that, at $Re = 950$ (Figure 23), the low fidelity shear stress is far from capturing the values of the high fidelity solution, which are well achieved with a surrogate high fidelity solution using just one high fidelity simulation in the reconstruction process.

4 BACKWARD FACING STEP

4.1 DESCRIPTION OF THE FLOW

The problem under consideration is the *2D* motion field that occurs when a fluid flow encounters a backward facing step. The case is bidimensional, incompressible and turbulent. We are interested in mean quantities, wich are obtainable by *RANS* system of equations (8). We have used the *SimpleFoam* solver with the turbulence modelling option enabled in order to find a stationary solution. The simulations are more demanding compared to the cavity case and, beacause of that, they have been performed in parallel mode distributing the load on four *CPU* cores.

The domain is a simple geometry of a step made up of two parts: an inlet box, $5\,m \times 1\,m$, and an outlet box, $20\,m \times 2\,m$, as we can see in Figure 28. The domain is generated with the *blockMesh* utility in OpenFoam using three blocks: the first block corresponds to the inlet box, while the other two blocks correspond, considering the outlet box splitted into two equal parts by an horizontal line, to the upper half and to the lower half of the outlet box. How the domain is created influence the sorting of the solution vectors but, as we experienced in the cavity case, sorting shouldn't condition the reconstruction process. The domain is represented in a cartesian coordinate system with the intersection point of the three blocks as the origin.

From the solution we expect a recirculation region behind the step due to the flow separation, as we can see in Figure 29.

4.2 LOW FIDELITY AND HIGH FIDELITY SIMULATIONS

The characteristics of a high fidelity simulation are:

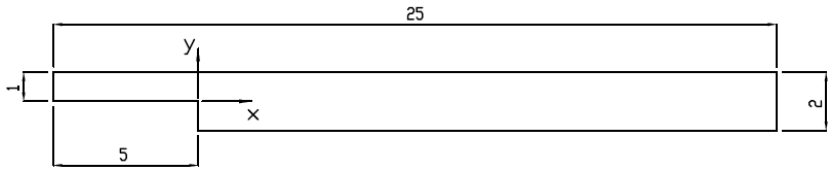

Figure 28: Geometry of the domain.

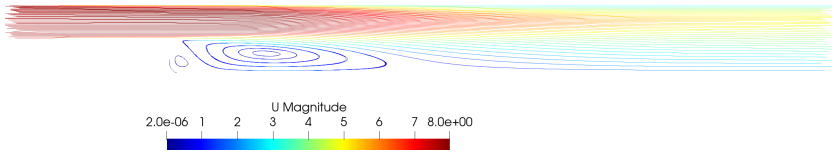

Figure 29: Visualization of streamlines at $Re = 38000$.

- a much more thicker mesh than the one from the low fidelity simulation. The inlet box contains 480×96 cells, the outlet box contains 1920×192 cells, with 414720 total cells and a cell side of $1/96\,m$;
- the use of a k-ωSST turbulence model, wich should work better in a separation framework;
- in most of the simulations the first cell is contained in the inner layer of the boundary layer, so the boundary layer is fully resolved.

On the other hand, the characteristics of a low fidelity simulation are:

- a coarse mesh where the inlet box contains 60×12 cells, the outlet box contains 240×24 cells, with 6480 total cells and a cell side of $1/12\,m$;
- the firts cell contained in *log-law* region of the boundary layer, so *wall functions* are needed and the boundary layer is not fully resolved;
- the use of a k-ε turbulence model.

The low fidelity mesh and the high fidelity mesh are represented in Figures 30 and 31. The Reynolds number is in the range $(5000 \div 50000)$ and it is used to calculate inlet condition for U. So, inlet boundary conditions are:

- $U = vRe/L$, with $v = 2 \cdot 10^{-4}\, m^2/s$ and $L = 1\, m$, which is the charateristic length of the flow,
- k calculated from equation (13) assuming a turbulent intesity $I = 0.05$ at the inlet,
- ϵ calculated from equation (14) in the k-ε model case,
- ω calculated from equation (18) in the k-ω model case,
- *zeroGradient* condition for the pressure.

Wall boundary conditions for the low fidelity simulations are:

- *no-splip* condition for the velocity,
- k calculated using *kqRWallFunction*,
- ε calculated using *epsilonWallFunction*,
- *zeroGradient* condition for the pressure.

Wall boundary conditions for the high fidelity simulations are:

- *no-splip* condition for the velocity,
- ω calculated using *OmegaWallFunction*, suitable at any y^+,
- $k = 0\, m^2/s^2$ if $Re < 30000$ or k calculted using *kLowReWallFunction* if $Re > 30000$,
- *zeroGradient* condition for the pressure.

Outlet boundary conditions are:

- *zeroGradient* condition for U, ω, k, ε,
- $p = 0\, m^2/s^2$.

Initial conditions are:

- $U = 0\, m/s$, $p = 0\, m^2/s^2$,
- k, ε, ω equal to the inlet value.

Using a residual control on the scaled residuals of 10^{-2} on p and 10^{-3} on $\boldsymbol{U}$, a low fidelity simulation will converge in approximately 3 seconds, while a high fidelity simulation will converge in approximately 1100 seconds.

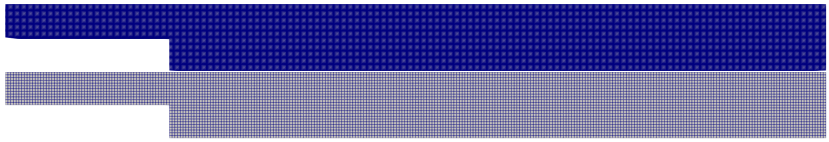

Figure 30: Difference about the high fidelity mesh and the low fidelity mesh.

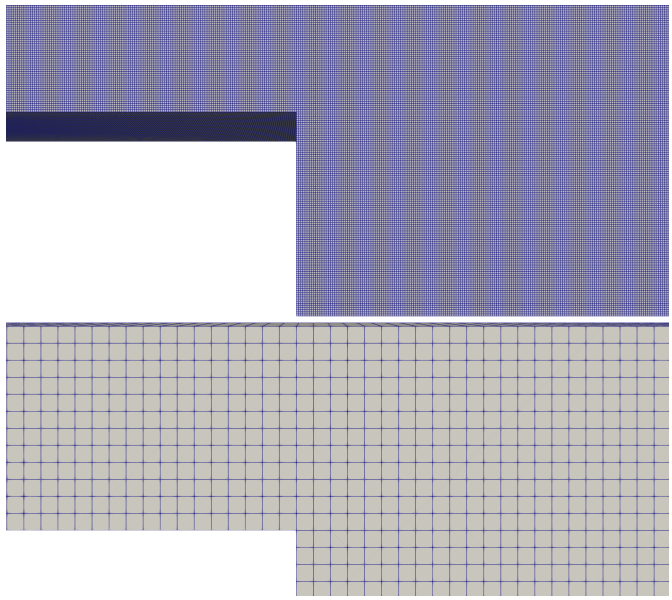

Figure 31: Detail about the difference of the two mesh.

4.3 RECONSTRUCTION

We performed 73 low fidelity simulations with Reynolds number in the range $(5000 \div 50000)$, each Re spaced apart from the previous one by a $\Delta Re = 625$. We have reconstructed three high fidelity surrogate simulations:

- $Re = 7000$,
- $Re = 13000$,
- $Re = 38000$.

These did not belong to the initial low fidelity simulations database. For each of them we have used a number of high fidelity simulations in the reconstruction process between 1 and 20. The reconstruction of the kinematic pressure and the reconstruction of the velocity are performed independently as described in the cavity case. The results are visualized in *Paraview* and represented in Figures 32-43. In all the screens, from top to bottom, there is:

- the true high fidelity simulation,
- a surrogate high fidelity simulation obtained using twenty high fidelity simulations,
- a surrogate high fidelity simulation obtained using fifteen high fidelity simulations,
- a surrogate high fidelity simulation obtained using ten high fidelity simulations,
- a surrogate high fidelity simulation obtained using five high fidelity simulations,
- the corresponding low fidelity simulation.

To evaluate the velocity reconstruction more quantitatively we have considered two different velocity profiles: the first one is the horizontal velocity along a vertical line at $x = 3\,m$ and the latter is the vertical velocity along a horizontal line at $y = -0.5m$. They are represented, for $Re = 7000$, $Re = 13000$ and $Re = 38000$, from figure 44 to Figure 49.

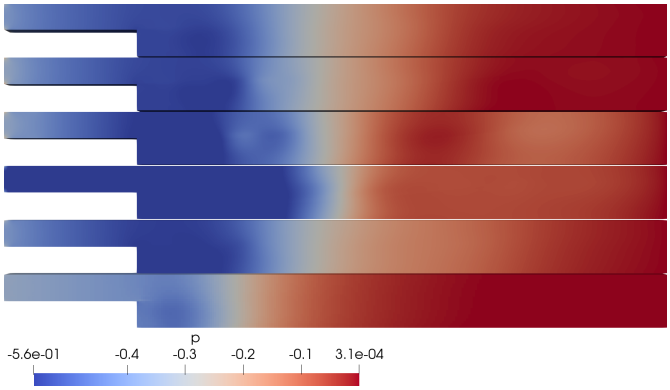

Figure 32: Paraview screen of the kinematic pressure reconstruction at $Re = 7000$.

Wall shear stress, represented in Figures 50-52, is evaluated at the bottom of the outlet box in each of the three cases. The trend is similar and shows a positive region from $x = 0\,m$ to $x = 2\,m$ approximately, corresponding to the secondary small recirculation bubble, and a wide negative region until $x = 11\,m$ at $Re = 7000$, $x = 10\,m$ at $Re = 13000$ or $x = 9\,m$ at $Re = 38000$, corresponding to the big recirculation bubble. Than the the wall shear stress becomes positive beacause of the reattachment of the flow. The main and the secondary ricirculation bubbles are clearly visible in the streamlines visualization in Figure 29. The low fidelity simulation is so coarse that can't detect the secondary corner eddy.

The same errors definitions illustrated in section 3.5 have been used.

4.4 COMMENTS

From the analysis of the results, we note that the errors are lower in the case at $Re = 38000$ for both velocity and pressure. This is reasonable beacause, as we can see from Paraview screens, low fidelity simulations behave closer to the high fidelity ones compared to the other two cases (see Figures 41-37 and 34). Considering pressure reconstruction at $Re = 7000$, visible in Figure 32, we can see that the low fidelity pressure field is quite

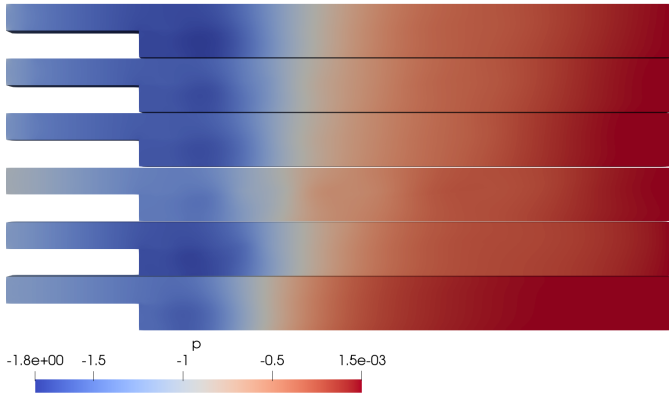

Figure 33: Paraview screen of the kinematic pressure reconstruction at $Re = 13000$.

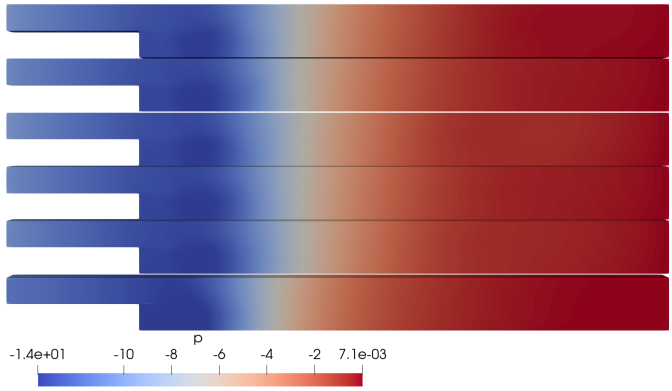

Figure 34: Paraview screen of the kinematic pressure reconstruction at $Re = 38000$.

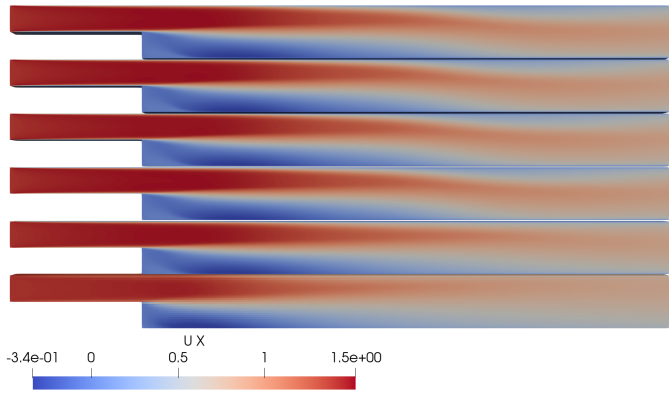

Figure 35: Paraview screen of the horizontal velocity reconstruction at $Re = 7000$.

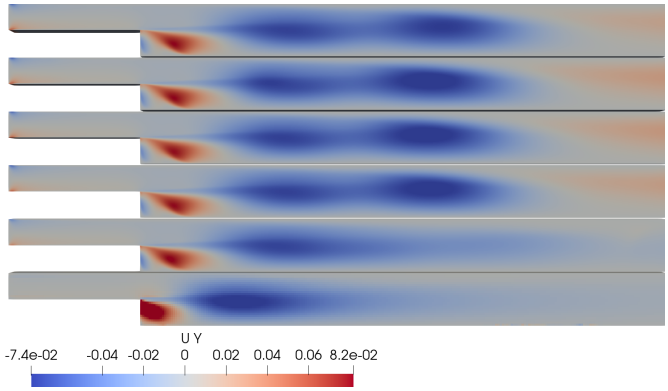

Figure 36: Paraview screen of the vertical velocity reconstruction at $Re = 7000$.

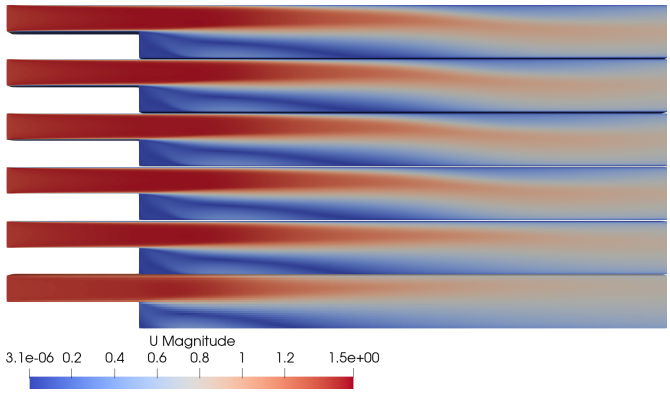

Figure 37: Paraview screen of the velocity magnitude reconstruction at $Re = 7000$.

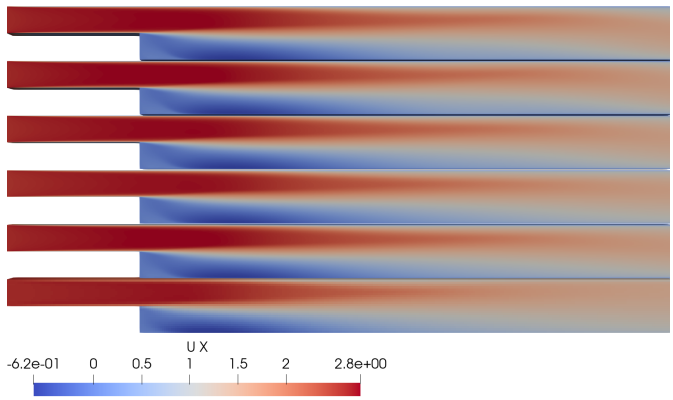

Figure 38: Paraview screen of the horizontal velocity reconstruction at $Re = 13000$.

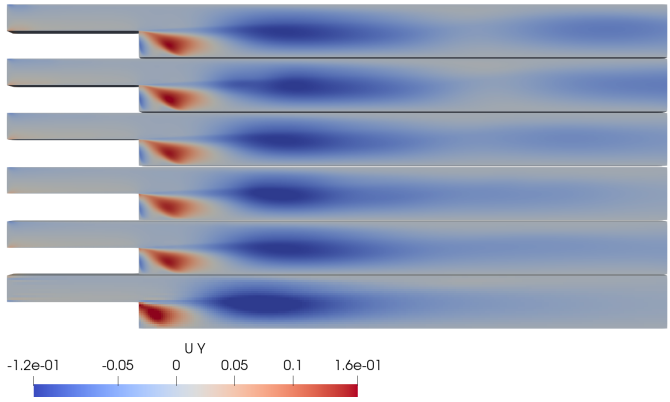

Figure 39: Paraview screen of the vertical velocity reconstruction at $Re = 13000$.

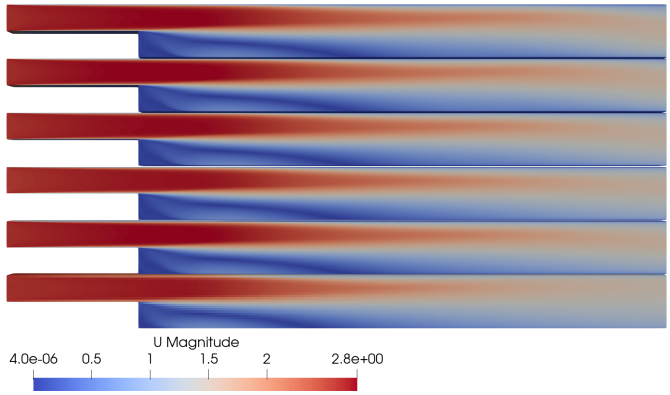

Figure 40: Paraview screen of the velocity magnitude reconstruction at $Re = 13000$.

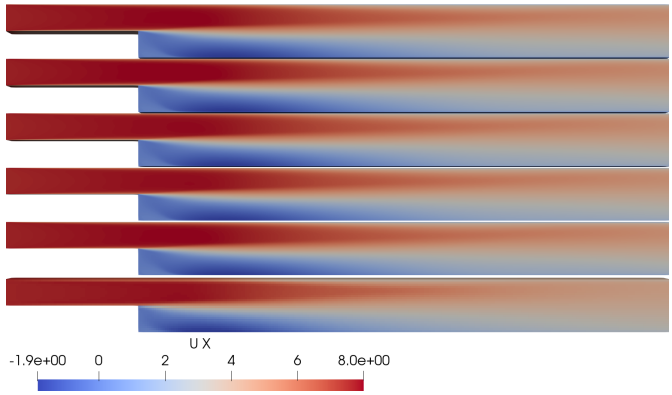

Figure 41: Paraview screen of the horizontal velocity reconstruction at $Re = 38000$.

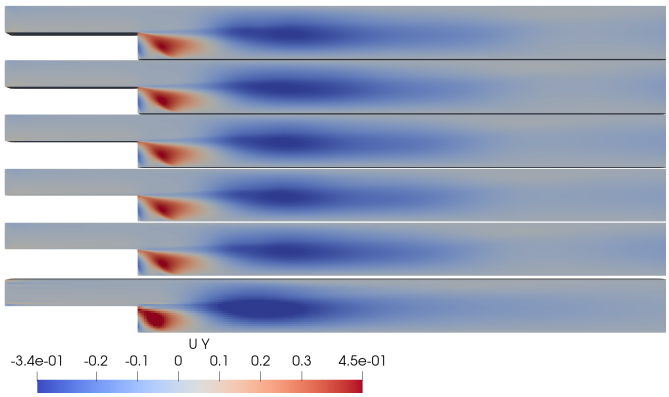

Figure 42: Paraview screen of the vertical velocity reconstruction at $Re = 38000$.

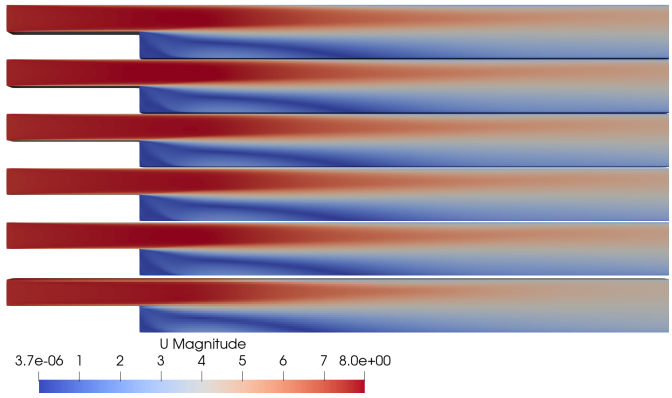

Figure 43: Paraview screen of the velocity magnitude reconstruction at $Re = 38000$.

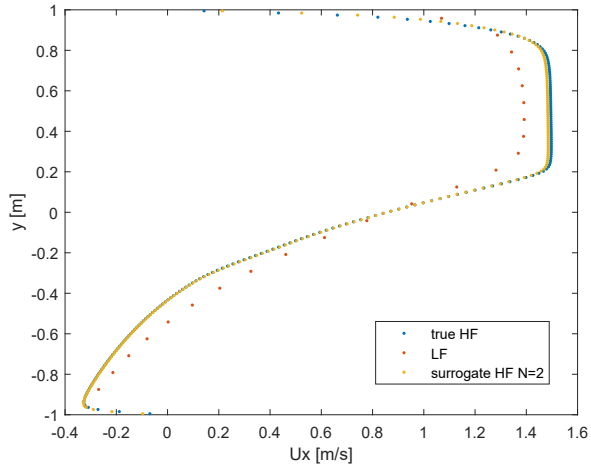

Figure 44: Horizontal velocity along a vertical line at $x = 3\,m$ at $Re = 7000$.

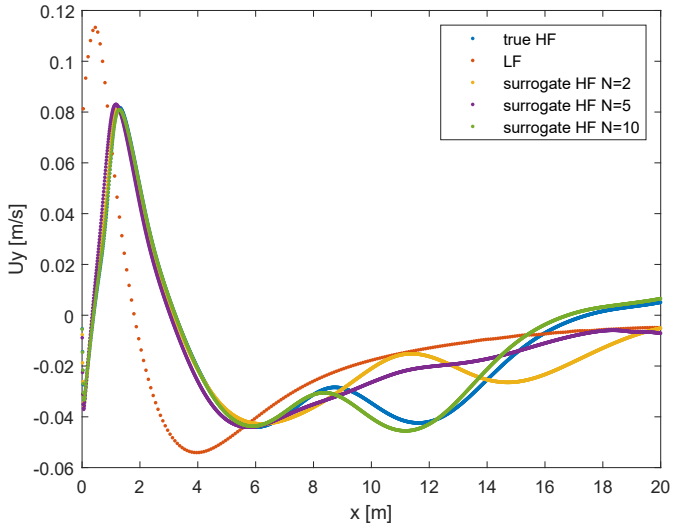

Figure 45: Vertical velocity along a horizontal line at $y = -0.5\,m$ at $Re = 7000$.

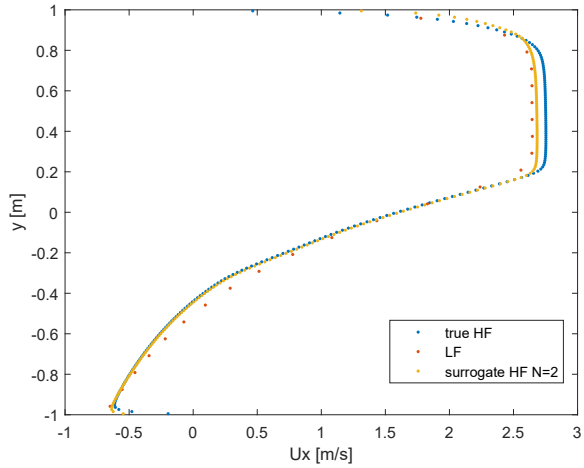

Figure 46: Horizontal velocity along a vertical line at $x = 3\,m$ at $Re = 13000$.

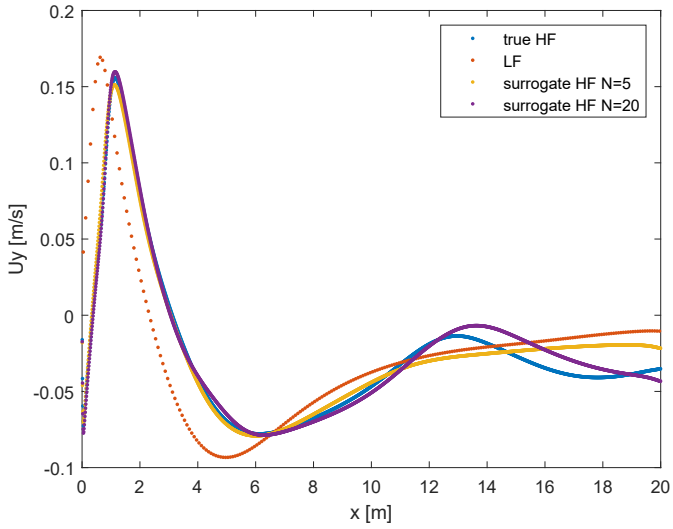

Figure 47: Vertical velocity along a horizontal line at $y = -0.5\,m$ at $Re = 13000$.

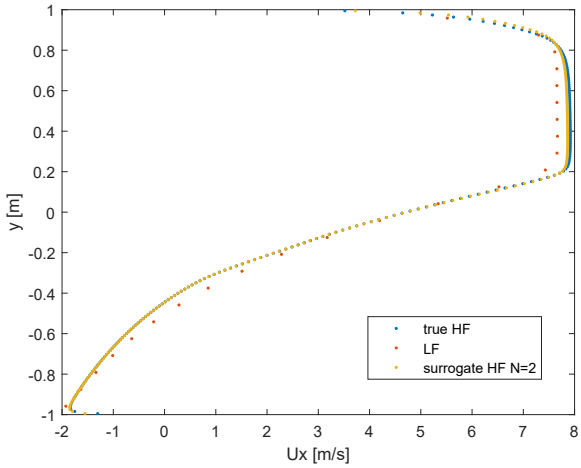

Figure 48: Horizontal velocity along a vertical line at $x = 3\,m$ at $Re = 38000$.

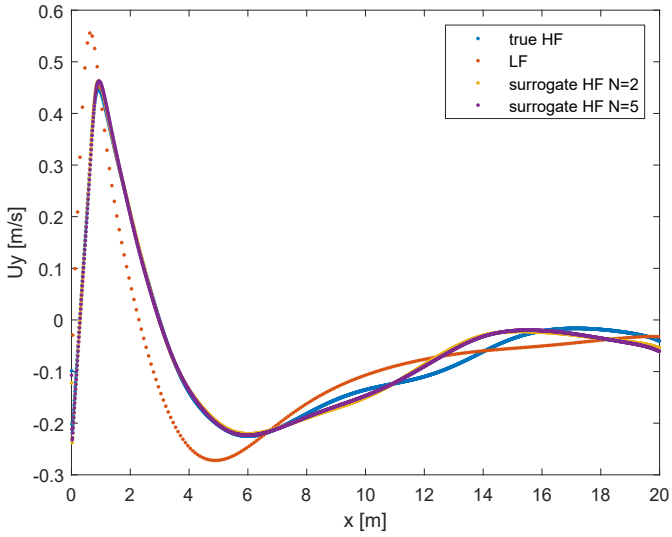

Figure 49: Vertical velocity along a horizontal line at $y = -0.5\,m$ at $Re = 38000$.

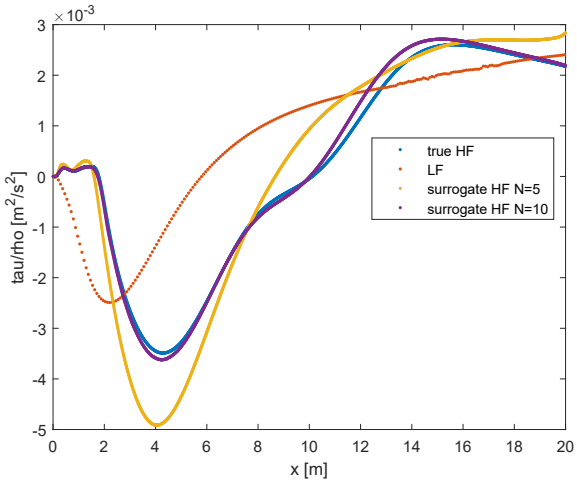

Figure 50: Wall shear stress at the bottom of the outlet box at $Re = 7000$.

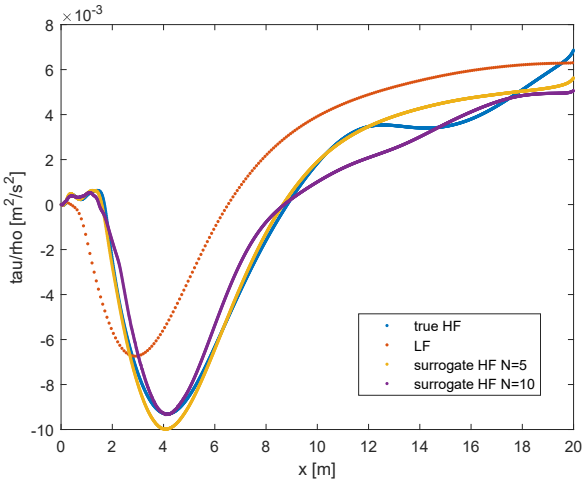

Figure 51: Wall shear stress at the bottom of the outlet box at $Re = 13000$.

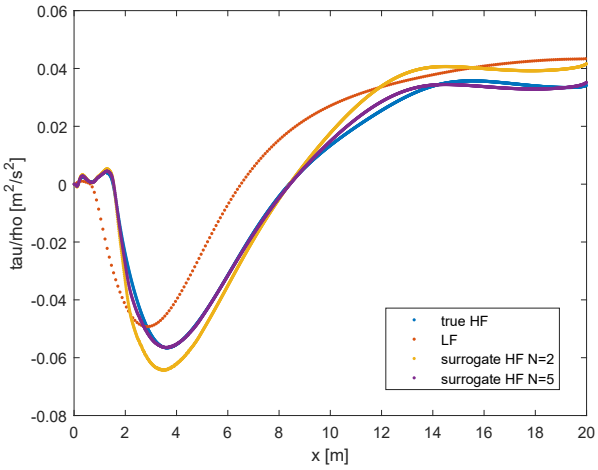

Figure 52: Wall shear stress at the bottom of the outlet box at $Re = 38000$.

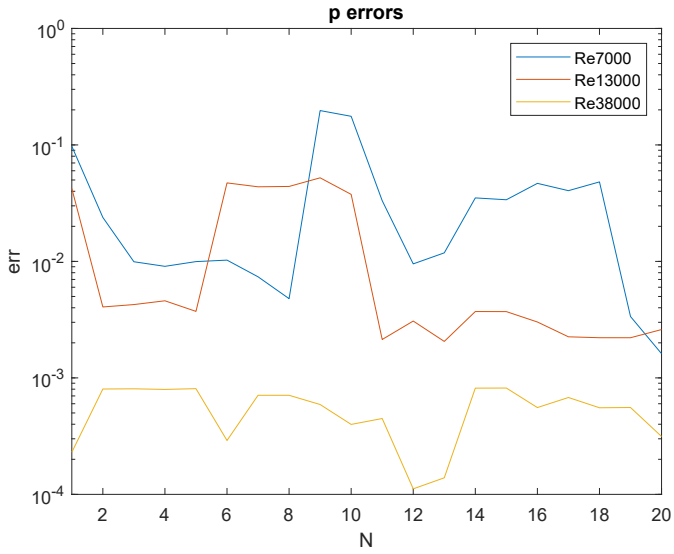

Figure 53: Adimensional error err_p of the surrogate kinematic pressure at different number N of high fidelity simulations used.

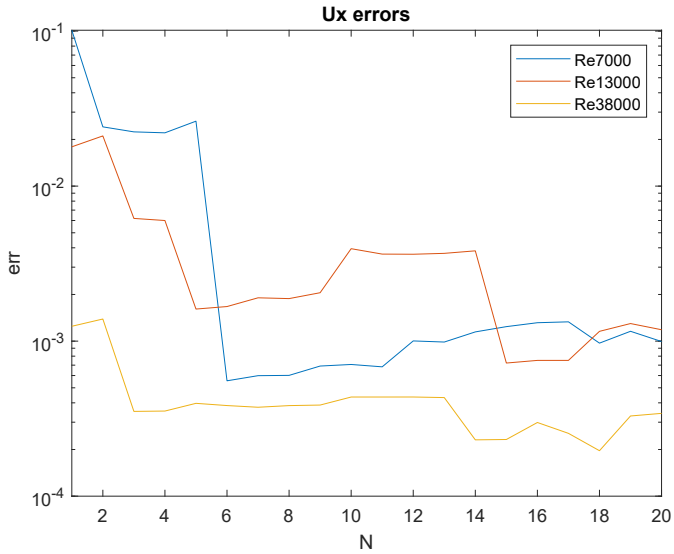

Figure 54: Adimensional error err_{U_x} of the surrogate horizontal velocity at different number N of high fidelity simulations used.

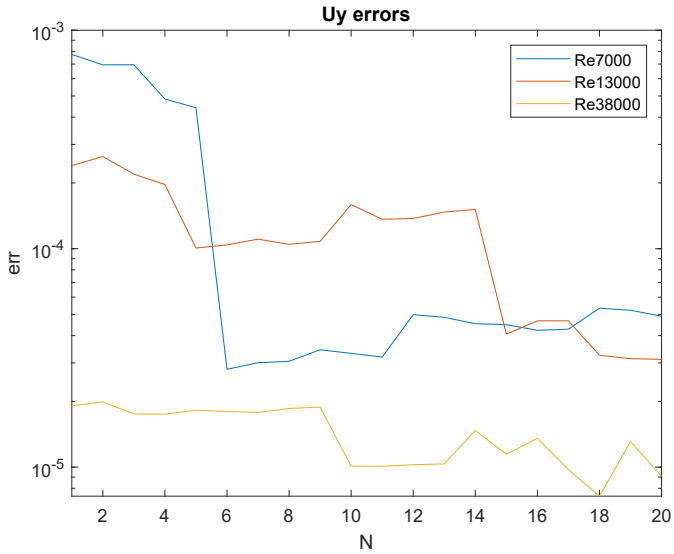

Figure 55: Adimensional error err_{U_y} of the vertical horizontal velocity at different number N of high fidelity simulations used.

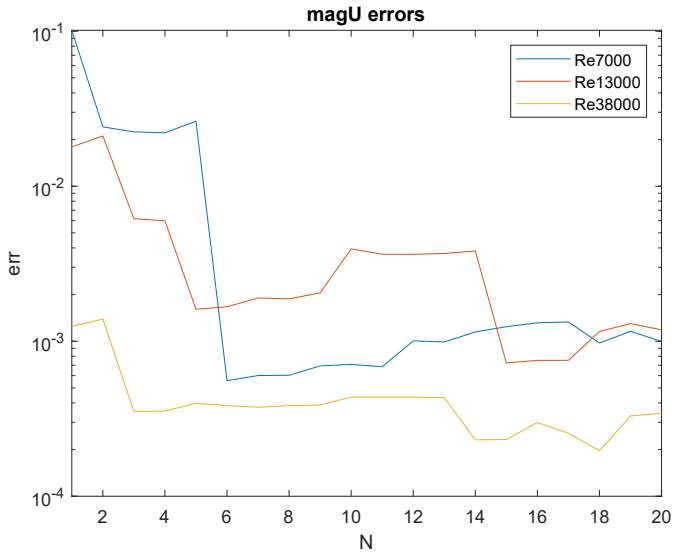

Figure 56: Adimensional error $err_{|\boldsymbol{U}|}$ of the velocity magnitude at different number N of high fidelity simulations used.

different from the high fidelity one and the recostruction is not perfect. The horizontal velocity and the velocity magnitude, visible in Figures 35 and 37, present some curvature that is totally neglected in the low fidelity case. Also the vertical velocity, visible in Figure 36, is characterized by some oscillations along the outlet box not detected by the low fidelity solution. This is also visible in Figure 47. These oscillations are not present in the case at $Re = 38000$, as we can see in Figure 41, in Figure 42 and in the plot 49.

Considering the reconstruction of kinetic pressure, as we can see in Figure 53, errors are characterized by incessant oscillations and a general trend not totally clear. Talking about velocity errors (Figures 54-56) we can see regions where the errors are almost constant, regions characterized by oscillations and regions where we can see a sharp decrease, especially at low N. The case is more complicated and the simple error decrease of the cavity case it is not present here.

Despite this, the reconstruction process works good in general: using $N = 10$ high fidelity simulations we can obtain a more than acceptable surrogate high fidelity simulation at $Re = 7000$, which is the worst case, where $N = 5$ are sufficient for $Re = 13000$ and

$Re = 38000$. The surrogate high fidelity simulations are also reliable in the evaluation of the wall shear stress, where the low fidelity simulations have incorrect results, as we can see in the plots 50 and 51.

4.5 A TRANSIENT TEST

Now we want to carry out a preliminary test of the reconstruction process applied to a transient *LES simulation* with a *Smagorinsky subgrid scale model* using the same backward facing step case. Simulate a turbulent flow through a large eddy simulation in a bidimensional case is not properly correct: turbulence is intrinsically three-dimensional because of the physical mechanisms that generate it, such as *vortex stretching* and *tilting*. On the other hand, a three-dimensional simulation is not a good test to start from due to the high computational cost. In fact, the physical accuracy does not play an important role in the validation of the reconstruction process: for our purposes, it is sufficient that the surrogate high fidelity simulation is close to a true high fidelity as much as possible. Also, to perform a correct *LES* it is suggested to resolve at least 80% of the turbulent kinetic energy and design consequently the grid. We are not going into these details in this preliminary test.

The grid used for the high fidelity simulations consists in an inlet box containing 160×32 cells and in an outlet box containing 640×64 cells, with 46080 total cells and a cell side of $1/32\,m$. The grid used for the low fidelity simulations consists in an inlet box containing 60×12 cells and in an outlet box containing 240×48 cells, with 6480 total cells and a cell side of $1/12\,m$. The boundary condition for p and $\boldsymbol{U}$ are the same as in the *RAS* case, while we will just use $k_{sgs} = 0$ at all the walls. The Reynolds numbers used are the same of the *RAS* case, the simulations are runned until $t = 40\,s$, where the flow is fully developed even at the lowest Reynolds numbers, and 80 equally spaced instants of time are stored.

The solver used in *Openfoam* to resolve the case is *pisoFoam*. Despite the numerical schemes involved are implicit, it is rec-

comended to verify the *Courant–Friedrichs–Lewy condition* to ensure accuracy, that is:

$$C = \frac{U_x \Delta t}{\Delta x} + \frac{U_y \Delta t}{\Delta y} \leq 1 \tag{33}$$

where Δt is the time discretization step, Δx and Δy are the spatial discretization steps. Since the velocity increases with the Reynolds number the discretization step chosen it is not the same for all the simulations and, as a consequence, also the execution time is different. The execution time for the low fidelity simulations is in the range $(100 \div 350)\, s$, while for the high fidelity simulations it is included in the range $(600 \div 2700)\, s$.

In this preliminary test, we will consider just $Re = 13000$ in the reconstruction process. The reconstruction process of a certain instant is performed using as input just the low fidelity simulations and the high fidelity simulations at the same time and each instant of time is reconstructed individually. The instants of time reconstructed are $t = 1\, s$, $t = 10\, s$ and $t = 40\, s$.

At $t = 1$ the reconstruction process works good and the first eddy detachment is captured. Here the low fidelity simulation depicts the behavior of the high fidelity solution. At $t = 10$ and $t = 40$ the surrogate high fidelity obtained is far from the true high fidelity and the errors are very high.

There are several problems; the first one is that, as we said, it involves transient solutions. We applied the reconstruction process at a a certain instant of time independently from the others, but this is applicable only if we are interested in the solution at one specific istant of time. If we are interested in all the temporal history of the solution we have to apply the reconstruction process at each temporal step: this is not applicable because each reconstruction will select a different set of high fidelity Reynolds numbers and the strategy loses the aim to keep as low as possible the number of high fidelity simulations to compute. An alternative is to concatenate all the solution arrays of the transient simulation into one and than apply the reconstruction process, but this seems to provide even worse results. Another problem is that, starting from a fluid at rest, the simulations at low Reynolds number evolve more slowly than the simulations at high Reinolds number. This means that, at a

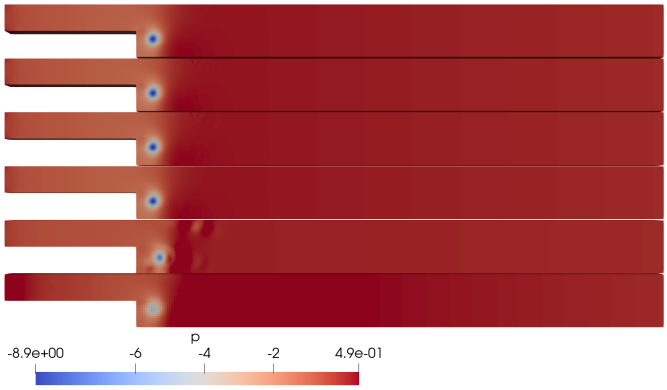

Figure 57: Reconstruction of the kinematic pressure field at $t = 1\,s$.

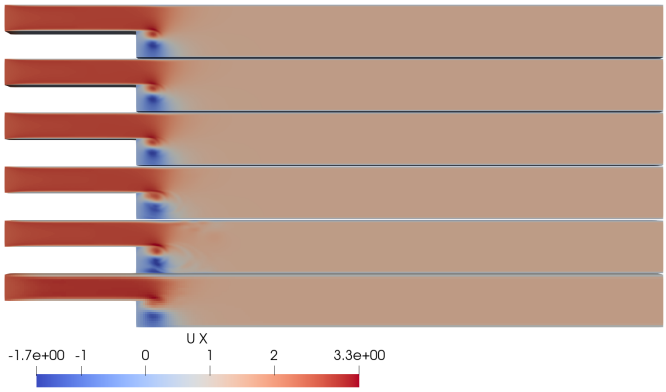

Figure 58: Reconstruction of the horizontal velocity at $t = 1\,s$.

certain time, we try to reconstruct a surrogate high fidelity simulation with some high fidelity simulations that include a large portion of fluid at rest and with some high fidelity simulations that are fully developed: this introduce spurious oscillations in the surrogate high fidelity. Eventually, *LES* simulations are intrinsically strongrly dependent on the grid adopted and, in this case, low fidelity simulations result so low on accuracy that they can't represent the behavior of the high fidelity solutions in the parameter domain. In the *Paraview* screens, represented in Figures 57-66, simulataions are ordered in the same way as before.

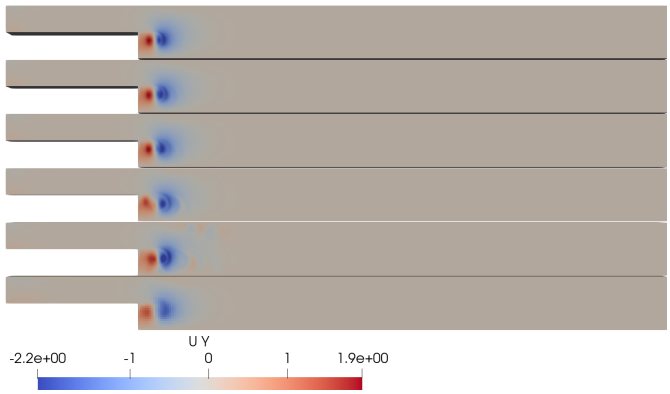

Figure 59: Reconstruction of the horizontal velocity at $t = 1\,s$.

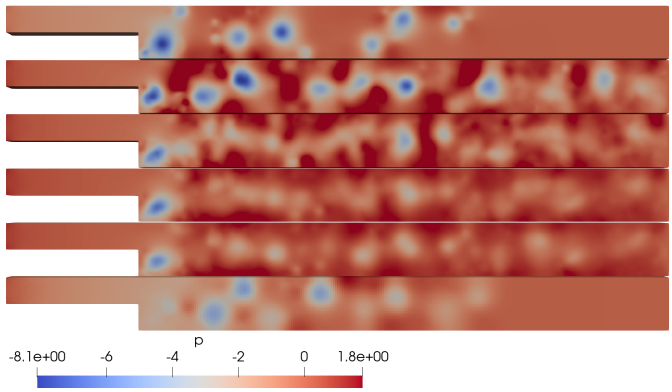

Figure 60: Reconstruction of the kinematic pressure field at $t = 10\,s$.

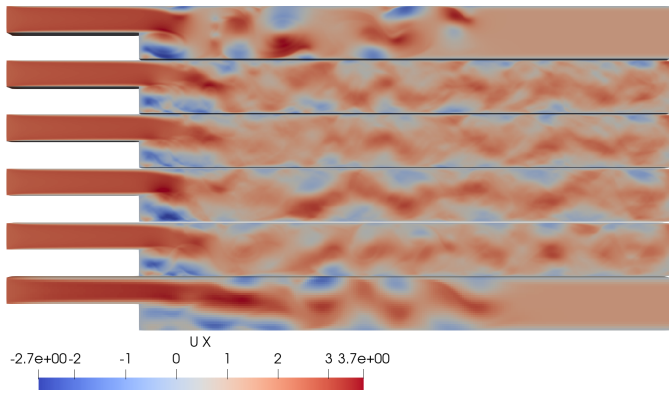

Figure 61: Reconstruction of the horizontal velocity at $t = 10\,s$.

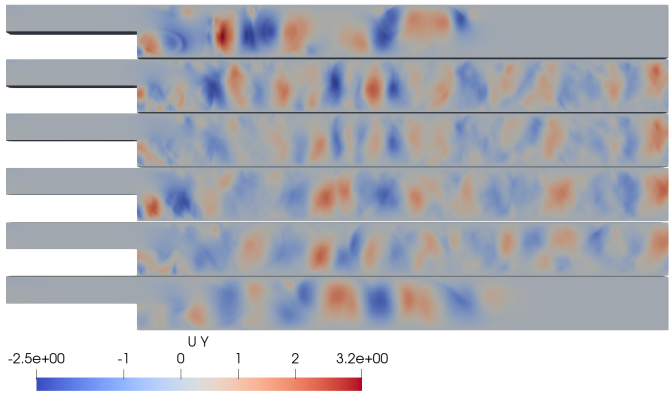

Figure 62: Reconstruction of the horizontal velocity at $t = 10\,s$.

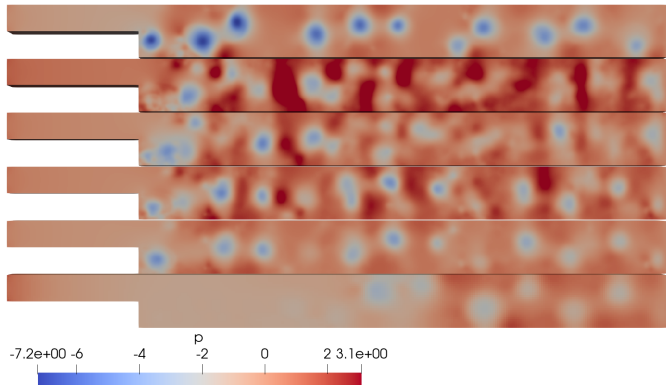

Figure 63: Reconstruction of the kinematic pressure field at $t = 40\,s$.

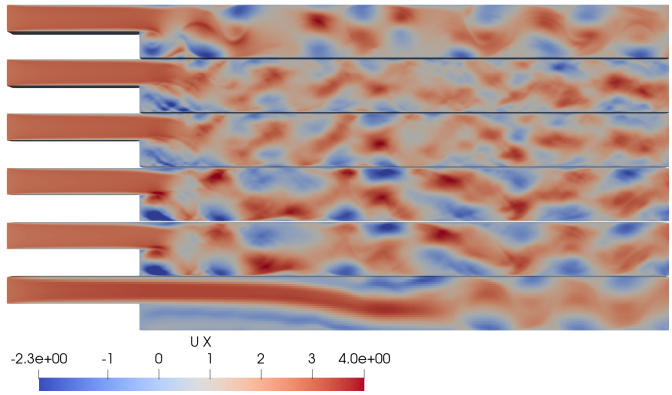

Figure 64: Reconstruction of the horizontal velocity at $t = 40\,s$.

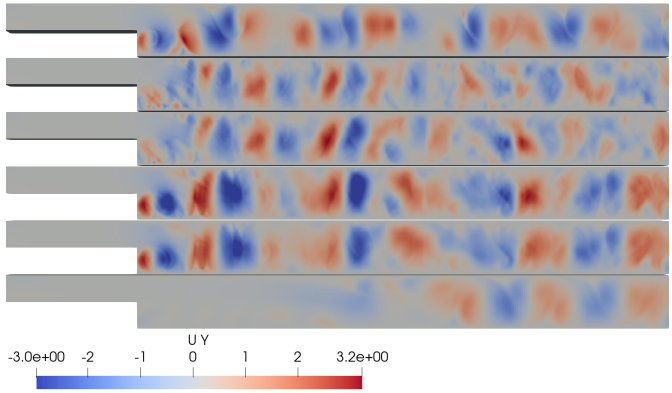

Figure 65: Reconstruction of the horizontal velocity at $t = 40\,s$.

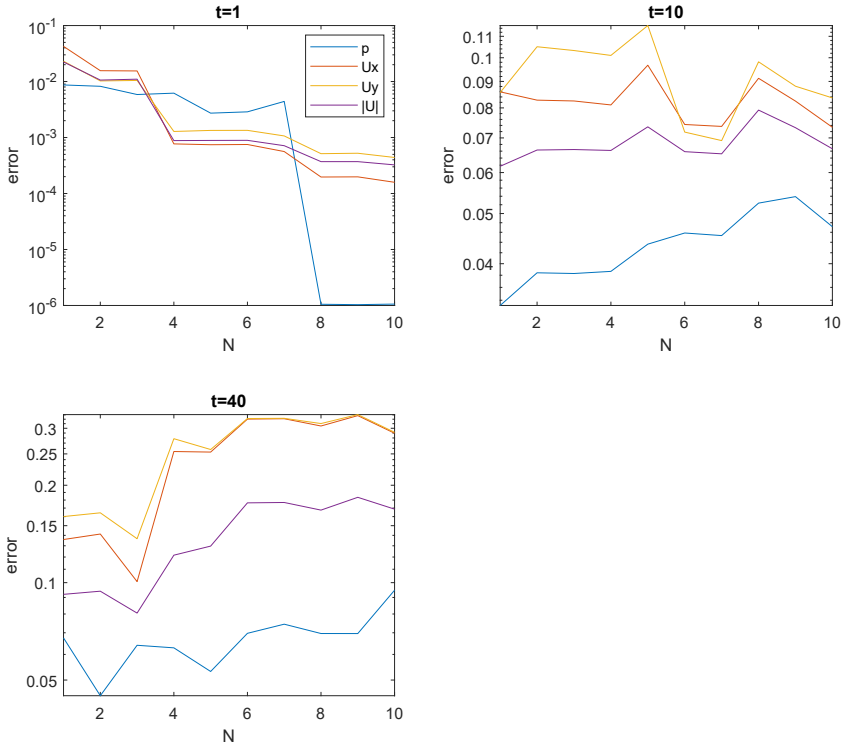

Figure 66: Reconstruction errors at different instant of times.

5 CONCLUSION

To summarize, we have applied the bifidelity strategy at:

- a stationary, laminar and bidimensional cavity flow,
- a *RAS* turbulence backward facing step,
- a *LES* turbulence backward facing step.

The firts case is simple, the solution obtained through the low fidelity simulations represent well the behavior of the high fidelity solutions in the parameter domain and the reconstruction process works very well. Using just three high fidelity simulations we can depict a surrogate high fidelity simulation in any point of the parameter domain.

The *RAS* backward step case introduces more complexity and, as it is imaginable, three high fidelity simulations are not sufficient to obtain a well reconstructed surrogate simulation, expecially at low Reynolds number where the low fidelity solutions departs from the high fidelity ones. Despite that, in most of the cases, five high fidelity simulations are sufficient and just at $Re = 7000$ the use of ten high fidelity simulations is recommended. We underline that the surrogate high fidelity simulation provides optimal results also for the wall shear stress, where the low fidelity one was incorrect. The execution time of a low fidelity *RAS* simulation is about $3\,s$, while for a high fidelity simulation it is around $1100\,s$: the approach is totally worth and we can reconstruct a surrogate high fidelity simulation in any point of the parameter domain at a computational cost comparable to a low fidelity simulation.

As we said the *LES* backward step case, which is the only transient case, runs into some problems. Probably a more accurate tuning of the low fidelity solutions could improve the results. Anyway, assuming that the reconstruction works, it could be useful just if we are interested in a specific istant of time, otherwise a different implementation of the bifidelity strategy is needed.

In conclusion, these tests show that this strategy is well suited for stationary problems and it could be particolary useful in those cases, such as more complicated optimizazion problems, where the behavior of the solution in the parameter domain is of interest to evaluate the point in the parameter space where the better performance or the better efficiency are reached. One thing that has to be taken into account, especially in three-dimensional cases, is the memory storage needed to save a high number of simulations as database.

BIBLIOGRAPHY

[Zhu-Narayan-Xiu] Xueyu Zhu, Akil Narayan, Dongbin Xiu *Computational Aspects of Stochastic Collocation with Multifidelity Models, SIAM Journal on Uncertainty Quantification, 2014.*

[Narayan-Gittelson-Xiu] Akil Narayan, Claude Gittelson, Dongbin Xiu *A stochastic collocation algorithm with multifidelity models, SIAM Journal on Scientific Computing, 2015.*

[Canuto-Pieraccini-Xiu] Claudio Canuto, Sandra Pieraccini, Dongbin Xiu *Uncertainty quantification of discontinuous outputs via a non-intrusive bifidelity strategy, Journal of Computational Physics, 2019.*

[Ghia-Ghia-Shin] U.Ghia, K.N.Ghia, C.T.Shin *High-Re solutions for incompressible flow using the Navier-Stokes equations and a multigrid method, Journal of Computational Physics, 1982.*

[Chien] Kuei-Yuan Chien *Predictions of Channel and Boundary-Layer Flows with a Low-Reynolds-Number Turbulence Model, AIAA Journal, 1982.*

[Wilcox-1] David C. Wilcox *Reassessment of the Scale-Determining Equation for Advanced Turbulence Models, AIAA Journal, 1988.*

[Wilcox-2] David C. Wilcox *Turbulence Modeling for CFD, 3rd edition, DCW Industries, 2006.*

[NASA resource] *NASA turbulence Modeling Resource.* https://turbmodels.larc.nasa.gov/

[Pope] Stephen B. Pope *Turbulent flows, Cambridge University Press, 2000.*

[Spalding] D. B. Spalding *A Single Formula for the "Law of the Wall", Journal of Applied Mechanics, 1961.*

[Smagorinsky] J. Smagorinsky *General circulation experiments with the primitive equations, 1963.*

[Zhiyin] Yang Zhiyin *Large-eddy simulation: Past, present and the future, Chinese Journal of Aeronautics, 2015.*

[Lesieur-Métais] M. Lesieur, O. Métais *New trends in large eddy simulations of turbulence, Annual Reviews Fluid Mechanics, 1996.*

[OpenFoam] *OpenFOAM-v2012 User Guide.* https://www.openfoam.com/documentation/user-guide/

[Barozzi] Giulio Cesare Barozzi *Matematica per l'ingegneria dell'informazione, Zanichelli, 2005.*